TEL AVIV UNIVERSITY

The Iby and Aladar Fleischman Faculty of Engineering

The Zandman-Slaner School of Graduate Studies

Effect of microvasculature diameter on ultrasound-mediated BBB opening

A thesis submitted toward the degree of

Master of Science in Biomedical Engineering

by

Sharon Katz

October 22

TEL AVIV UNIVERSITY

The Iby and Aladar Fleischman Faculty of Engineering

The Zandman-Slaner School of Graduate Studies

Effect of microvasculature diameter on ultrasound-mediated BBB opening

A thesis submitted toward the degree of

Master of Science in Biomedical Engineering

by

Sharon Katz

This research was carried out in the Department of Biomedical Engineering

Under the supervision of Dr. Tali Ilovitsh

October 22

Abstract

Blood brain barrier (BBB) opening using focused ultrasound (FUS) and microbubbles (MB) is an effective tool for therapeutic delivery to the brain. MB oscillations and concentration play a key-role in the success of BBB opening. Since effective BBB opening highly depends on MB oscillations, and since the brain vasculature is inherently heterogenic in diameter, reduced MB oscillations in smaller blood vessels, together with a lower number of MBs in capillaries, can lead to variations in BBB opening. Here, we established a method to characterize the extravasation of fluorescent molecules following FUS-mediated BBB opening as a function of microvasculature diameter, at a single blood vessel resolution. BBB opening was visualized using fluorescence microscopy, through Evans blue (EB) leakage, while blood vessels were marked by a second FITC-labeled dextran. A robust automated code was used to extract the blood vessel's morphological features and quantify the amount of extravasation as a function of blood vessel diameter. In the treated brains, EB extravasation increased as a function of blood vessel diameter. Moreover, the percentage of BBB opened blood vessels increased with blood vessel diameter. In conclusion, we find that larger capillaries are more prone to BBB opening. This could have major impact on therapeutic pharmacokinetics and limit the resulting outcomes, therefore the impact of blood vessel diameter should be considered when developing safe and reliable protocols for FUS-mediated BBB opening.

Table of contents

Abbreviations and symbols

BBB …….…… Blood-brain barrier	PNP ……..... Peak negative pressure
FUS ……..…… focused ultrasound	RF ……..…..... Radiofrequency
MB ……..…..……... Microbubble	FFT ……..…..... Fast-Fourier-transform
EB ……..…..... Evans-Blue	PCD ...…....… Passive cavitation detection
FITC …..……..... Fluorescein isothiocyanate	SCD ……..…….. Stable cavitation dose
IV ……...…....……..….. Intra-venous	ICD ……..…..... Inertial cavitation dose
BBBD ……... Blood-brain-barrier disruption	HPF …...……..…..... High-pass filter
MRI ….....…Magnetic resonance imaging	RMS …...……..…..... Root-mean-squared
US ...….....…ultrasound	MW ……...…..... Molecular weight
RPE ……..…..... Rayleigh-Plesset equation	PFA …...……..…..... Paraformaldehyde
$R\ [m]$ ……..... Bubble radius	γ……..…..…..…… Adiabatic index
P [Pa] ……..……...….. Pressure	β ..... Oscillator damping coefficient
$\rho_L\ [\frac{kg}{m^3}]$……..…… Liquid density	α …..…. Oscillator driving force coefficient
$\nu_L\ \left[\frac{kg}{m \cdot sec}\right]$ ……..….. Liquid viscosity	$\omega\ \left[\frac{rad}{sec}\right]$ ……..…….... Oscillation frequency
$\sigma\ \left[\frac{mN}{m}\right]$ ……....……... Surface tension	$\chi\ \left[\frac{mN}{m}\right]$ …..... elastic compression modulus
$k_s[s.p.]$ …..... surface dilatational viscosity	$c\ \left[\frac{m}{sec}\right]$ ……..…….…..... Speed of sound
ϵ……..... dimensionless constant	$w_i\ [\mu m]$ … Distance from vessel wall to perivascular area
η……..... dimensionless constant	$d\ [\mu m]$ …….. Perivascular area width
κ ……...…..… Polytropic index	

List of figures

List of Publications

- **S. Katz**, R. Zarik, Y. Hagani and T. Ilovitsh, “Ultrasound-mediated blood brain barrier opening is affected by vasculature diameter”. Under review (2022).
- M. Bismuth, **S. Katz**, H. Rosenblatt, M. Twito, R. Aronovich and T. Ilovitsh. Acoustically Detonated Microbubbles Coupled with Low Frequency Insonation: Multiparameter Evaluation of Low Energy Mechanical Ablation. Bioconjug. Chem. (2021).
- M. Bismuth, **S. Katz,** T. Mano, R. Aronovich, D. Hershkovitz, A. Exner and T Ilovitsh. Low frequency nanobubble-enhanced ultrasound mechanotherapy for noninvasive cancer surgery. Nanoscale (2022).

Conference presentations:

- **S. Katz,** “Effect of Microvasculature Diameter on FUS-Mediated BBB Opening”, IEEE IUS, October 2022. (Poster presentation)

- **S. Katz**, "Effect of microvasculature diameter on ultrasound-mediated BBB opening", Department seminar, Department of Biomedical Engineering, Tel Aviv University, Israel, May 2022. (Oral presentation).

1 Introduction

The BBB is a unique formation that selectively restricts substance exchanges between the circulatory system and the brain parenchyma. The BBB plays a significant role in preventing pathogenic contamination of the brain; however, it also poses serious limitations on neurological treatment as it prevents most drugs from reaching the brain[1].

Recently, advances in therapeutic ultrasound introduced a novel mechanism by which the BBB can be temporarily and locally disrupted. This mechanism relies on focused ultrasound (FUS) sonication of microbubbles (MB) that normally act as ultrasound contrast agents (UCA). The MB are intravenously (IV) injected to the patient, and upon sonication, cavitate and exert mechanical force on the surrounding vessel wall, therefore increasing its permeability[2]. Since its inception, FUS-mediated BBB disruption (BBBD) was demonstrated in-vivo in model animals, and recently also in humans[3–6]. However, it was recently shown that MB cavitation, which is a key element of FUS-mediated BBBD, varies with respect to the diameter of the containing vessel[7–9].

In this work, we examine the relationship between capillary diameter and the efficiency of FUS-mediated BBBD. For this propose we establish a novel method that enables the assessment of FUS-mediated BBBD at a single blood-vessel resolution. Furthermore, we use a tissue mimicking phantom to explore the differences in MB cavitation within tubes of variable diameters. According to our in-vitro results, we suggest that the variations in FUS-mediated BBBD could be the result of the restriction of MB cavitation within small tubes.

2 Research objectives

This work was aimed at examination of variations in FUS-mediated BBBD with respect to blood vessel diameter. Therefore, the first objective of this research was to

understand the underlying mechanism by which the blood vessel diameter could cause a variation in FUS-mediated BBBD. For this purpose, we needed to design an in-vitro setup where we could examine the cavitational response of MB to FUS in tissue mimicking phantoms. After establishing an appropriate setup where reliable metrics for MB cavitation can be measured, we wished to measure the cavitational response of MB in synthetic capillaries of different diameters and preform a thorough comparison.

We then sought to examine the effects of vessel diameter on FUS-mediated BBBD in-vivo. To do so, we first needed to establish a reliable system for FUS-mediated BBBD in-vivo. After achieving this milestone, the next goal was to develop a method for quantitative assessment of the extant of BBBD in a single blood-vessel resolution. This method was designed to also enable the extraction of vascular morphological features, and most importantly the vessel diameter. Once a reliable method was established, sufficient data needed to be gathered to perform a statistical comparison of the extant of FUS-mediated BBBD with respect to vessel diameter.

3 Theoretical Background

This thesis presents a method that was developed in order to assess variations in FUS-mediated BBBD as a function of microvasculature diameter. In this section, we will discuss the different aspects of this therapeutic method. First, we will present the BBB, in order to provide a better understanding of the motivation behind FUS-mediated BBBD. Thereafter, we will present the physical concepts upon which this method relies. We will discuss both the basic concepts of ultrasound as a tool for imaging and therapy, and the concept of MB-enhanced ultrasound. By this point the underlying mechanism for FUS-mediated BBBD

should be clearer to the reader and a deeper dive could be taken into the open questions whose answers we pursued in this work.

3.1 The blood-brain-barrier

The brain is arguably the most important organ in our body and is responsible for much of our metabolic consumption[10]. To provide the brain with sufficient amount of nutrients, a dense network of blood vessels is required, of which the most predominant are the capillaries[11]. The capillaries are also where most of the substance exchange between the blood and tissue occurs. Brain capillaries differ from capillaries in other bodily regions by being closely enveloped with multiple cells, forming together the "neurovascular unit". Furthermore, studies show that the tight junctions of the endothelial cells that form the brain capillaries are more restrictive than their counterparts in other bodily regions[12]. These unique microvasculature features contribute to the construct of the blood-brain-barrier (BBB) which limits substance exchange between the vascular system and the brain parenchyma.

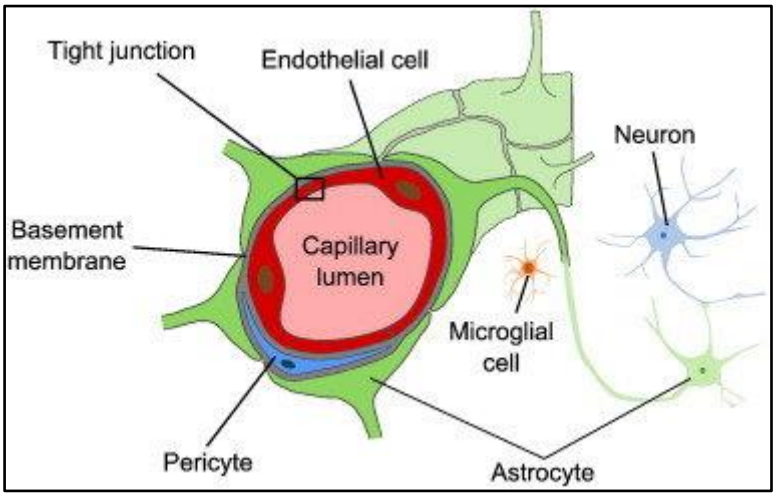

Figure 1: The neurovascular unit is composed of multiple cells surrounding the brain capillary. Together with the restrictive tight-junctions they form the blood-brain barrier (BBB). Illustration adopted from Heye et. al. (2014) [13]

The BBB plays a critical role in protection of the brain from pathogen infiltration, and it also helps sustain the very gentle chemical homeostasis required to maintain brain function.

Alongside its functional importance, the BBB also imposes a very harsh constrain on treatment of neurological diseases and disorders, as it is impermeable to most pharmaceuticals[1].

Over the years, multiple approaches were suggested and examined, aiming to overcome the BBB and allow for drug delivery to the brain in a noninvasive manner. Most of these methods are pharmacological methods, which harness endogenous biological mechanisms for BBB crossing to deliver specific molecules[14]. While some of these are highly efficient, they lack both spatial and temporal specificity, thus exposing the entire brain to danger of contamination for a sustained period of time.

3.1.1 BBBD visualization and quantification

To determine the effectivity of any method for BBBD, a suitable measure for BBB integrity must be established. The earliest markers for BBB integrity were simple dyes, with the most common being EB. These dyes are injected to the model animal's blood stream and reach the brain vascular system. The dyes' molecular size and formulation are optimized so that they cannot cross an intact BBB but can perfuse out when the BBB is breached[15], therefore, the appearance of the dye in the brain parenchyma can indicate a breaching of the BBB. The extravasation of these markers into the brain parenchyma is measured ex-vivo, either by digital image processing of brain section microscopy slides, or by chemical extraction of the dye followed by volumetric quantitation of the extracted dye[16].

More recently, magnetic resonance imaging (MRI) contrast agents, such as Gadolinium, also became popular in visualization and quantification of BBBD. The perfusion of these agents into the parenchyma upon BBBD can be visualized in-vivo in real-time, so that temporal information regarding the process can be acquired as well[17,18].

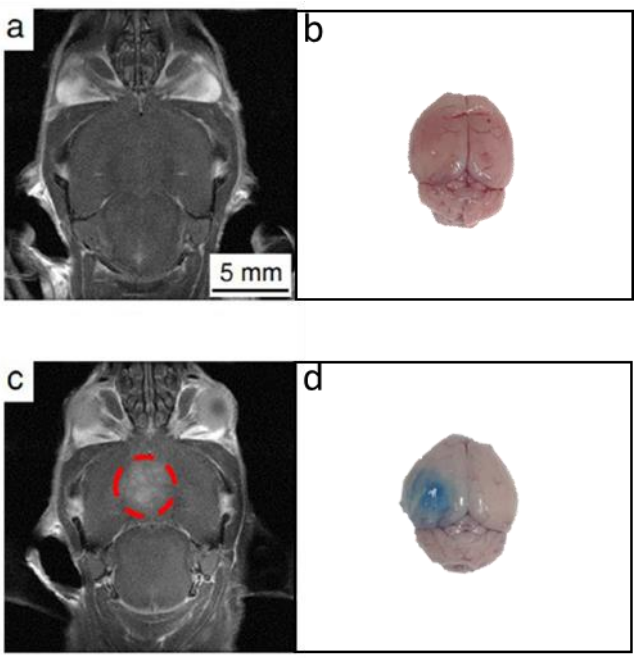

Figure 2: BBB opening can be visualized and quantified in real-time using Gadolinium-enhanced MRI (a, c, adopted from Ilovitsh et al.[19]) , or ex-vivo using dyes such as EB (b, d). (a, b) show no sign of BBB opening, whereas (c, d) indicate a disrupt BBB.

3.2 Ultrasound principles

Ultrasound (US) is a general term describing sound waves with frequencies that exceed the human hearing limit of 20 kHz. US, much like regular sound, is carried by pressure waves, meaning it induces variations in pressure across the medium in which it propagates. An important feature of US radiation is that it is non-ionizing and safe; furthermore, US has relatively good penetration depth in soft tissues. Due to these properties, and due to the low cost of US transducers, US gained great popularity as an imaging modality for various clinical applications.

The main component of an US system is the US transducer, which is composed of a single or multiple piezoelectric elements. A piezoelectric element is able to convert alternating electric voltage into a pressure wave, and vice versa. In an US imaging system, the transducer is driven by a function generator to produce short acoustic pulses, which can be directed at a specific region of interest. When an US wave encounters a scatterer, it can be

absorbed, reflected, or scattered. Whenever the US wave is reflected from a scatterer, it creates an echo that travels back towards the transducer. The transducer then converts the acoustic echo to an electric signal. By measuring the time from transmission to echo receiving, the scatterer can be spatially localized, and an image can be reconstructed.

If the US wave is absorbed rather than reflected, it causes vibration of particles within the scatterer, resulting in temperature increase. The thermal effect of US is known for many years and was suggested as a therapeutic tool almost 100 years ago[20]; it has since been used for various applications, including thermal ablation of tumors, wound healing and pain modulation[21].

Besides the thermal effect, US was also shown to induce non-thermal effects within the sonicated medium. The non-thermal effects of US are normally divided in two: acoustic streaming, and acoustic cavitation. Streaming is described by changes in fluid flow caused by the US wave; these changes may be macroscopic (e.g., changes in blood flow) or microscopic (e.g., changes in flow through cell membranes), also known as microstreaming. The second non-thermal effect of US is acoustic cavitation, that is, compression and relaxation of gas bubbles within the medium, caused by the local changes in pressure[22]. The thermal and non-thermal effects of US often appear together, but the dominance of each effect can be modulated by the US parameters (e.g., intensity and frequency) and by characteristics of the treated medium (e.g., water and protein content)[21].

3.2.1 Low frequency focused ultrasound

In recent years, focused ultrasound (FUS) at low frequencies (below 650 kHz) was developed as a way to deliver large quantities of energy to specific regions of the brain. At these low frequencies the attenuation of the US wave is minimal, thus it can easily penetrate an intact human skull[23,24]. FUS-mediated thermal ablation has been used to treat over 500 patients for

brain indications including brain tumors, essential tremor, psychiatric applications, chronic pain and epilepsy[25].

3.3 Acoustic cavitation

An important mechanism by which US interacts with the sonicated medium or tissue is induction of acoustic cavitation. The basis of acoustic cavitation lies in the fact that gas has much higher compressibility compared to liquid, thus we can neglect the compression of the liquid and derive a formulation of the dynamics of a single gas bubble in a liquid medium. Considering mass and momentum conservation alone, we can derive the following equation[26]:

$$R\ddot{R} + \frac{3}{2}\dot{R}^2 = \frac{P(R) - P_\infty}{\rho_L} \quad (1)$$

Where R is the bubble radius, ρ_L is the liquid density, P_∞ is the liquid pressure at an infinite distance from the bubble and $P(R)$ is the liquid pressure just outside the bubble. Note that this model assumes isothermal compression of the gas within the bubble.

Later modifications to equation (1) were preformed over the years, with the most profound being the introduction of the liquid viscosity (ν_L), the gas pressure inside the bubble (p_B) and the bubble surface tension (σ) into the equation, yielding the *Rayleigh-Plesset equation (RPE)*[27]:

$$R\ddot{R} + \frac{3}{2}\dot{R}^2 = \frac{1}{\rho_L}\left\{P_B(t) - P_\infty(t) - \frac{4\nu_L}{R}\dot{R} - \frac{2\sigma}{R}\right\} \quad (2)$$

Assuming the pressures P_B and P_∞ are constant, an equilibrium radius for the bubble can be derived:

$$R_0 = \frac{2\sigma}{P_B - P_\infty} \quad (3)$$

Where if the bubble initial radius is R_0 it will remain unchanged.

3.3.1 Linear cavitation

Having established equations (2) and (3), we can now use them to model the bubble's response to a driving pressure ($P_\infty(t)$), with the easiest form being a low amplitude sinusoidal pressure:

$$P_\infty(t) = P_\infty(1 + \epsilon \cdot \cos(\omega t)) \tag{4}$$

With ϵ being some small dimensionless constant, and ω being the oscillation frequency of the pressure wave. Under the assumption that the process is adiabatic, the ideal gas equation holds, thus we can write the gas pressure as:

$$P_B(t) = P_{B,0} \cdot \left(\frac{R_0}{R}\right)^{3\kappa} \tag{5}$$

Where $P_{B,0}$ is the gas pressure at equilibrium (when $R = R_0$), and κ being the *polytropic index* of the gas. κ may be replaced by the *adiabatic constant* of the gas, γ in the case that the process is adiabatic (no heat exchange between the bubble core and the liquid). Furthermore, under assumption that the changes in the gas pressure are small enough to be linearized by a Tailor's series, Plesset was able to show that the bubble radius formula takes the form of a damped linear harmonic oscillator:

$$\ddot{R} + 2\beta\dot{R} + \omega_0^2[R - R_0] = -\epsilon \cdot \alpha \cdot e^{i\omega t} \tag{6}$$

The solution for such an equation is a superposition of a damped harmonic term with frequency of ω_0, and a second harmonic term with frequency ω.This practically means that when we apply a sinusoidal driving pressure to the bubble the returning echoes will have both the driving frequency ω, as well as the natural frequency of the bubble, ω_0. The bubble natural frequency can also be derived:

$$f_0 = \frac{\omega_0}{2\pi} = \frac{1}{2\pi}\sqrt{3\kappa \cdot \frac{P_{B,0}}{\rho_L R_0^2} - \frac{2\sigma}{\rho R_0^3}} \tag{7}$$

A common approximation is that the surface tension is negligible compared to the gas pressure, hence (7) becomes:

$$f_0 = \frac{1}{2\pi}\sqrt{3\kappa \cdot \frac{P_{B,0}}{\rho_L R_0^2}} \tag{8}$$

Also known as *Minnaert's equation*[28]. For a bubble of air, with radius of 1 μm, preforming small, adiabatic oscillations in water at room temperature and atmospheric pressure, the natural frequency will thus be approximately 3.3 MHz[22].

3.3.2 Non-linear cavitation

By now we have discussed the easiest form of bubble cavitation, in which the driving pressure is small enough so that the bubble acts as a linear oscillator. Now, let us reintroduce a general sinusoidal driving force into RPE:

$$R\ddot{R} + \frac{3}{2}\dot{R}^2 = \frac{1}{\rho_L}\left\{P_{B,0} \cdot \left(\frac{R_0}{R}\right)^{3\kappa} - P_\infty(1 + \eta \cdot \cos(\omega t)) - \frac{4\nu_L}{R}\dot{R} - \frac{2\sigma}{R}\right\} \tag{9}$$

This general case, where the driving force, here noted as η, is not small, is harder to solve analytically, but both numerical analysis and experimental observations show that the bubble here has multiple oscillation frequencies other than the frequency of the driving force[27].

3.3.3 Inertial cavitation

There are two important aspects of RPE that haven't been discussed in the previous sections. The first being the clear notion that it contains a singularity at $R = 0$. However, this singularity is prevented by the gas pressure term, P_B, that may increase indefinitely as the radius decreases (as seen in equation (5)). More importantly, dynamic analysis of this equation shows that the oscillations may only be stable for certain equation parameters ($P_{B,0}$, $P_\infty(t)$, ν_L, R_0), whereas a different choice of parameters, RPE yields an explosive growth of

the bubble ($R \to \infty$)[29]. In this case, the bubble becomes unstable and can no longer be described by the equations above[30].

In reality, when a bubble exceeds a certain size, the liquid pressure forces its collapse, this phenomenon is referred to as unstable cavitation or inertial cavitation, due to the dominance of inertial forces during the bubble collapse[30]. A bubble collapse is accompanied by the emission of a destructive shockwave throughout the surrounding liquid, the effects of which were studied intensively over the years[31]. Given that the properties of the bubble ($P_{B,0}$, R_0), and the properties of the liquid (ν_L) are constant, one might try to find a threshold for the driving pressure $P_\infty(t)$ that would separate stable cavitation from inertial cavitation. Indeed, various expressions for such threshold were proposed over the years, most of which are derived from the works of Francis Blake[32]; a detailed discussion of these thresholds was given by Robert Apfel (1981)[33].

3.3.4 Liquid evaporation

It is important to note that some papers refer to cavitation as the process by which a bubble of vapor is created within a liquid upon intense pressure reduction[34]. Indeed, the induction of local pressure decrease, whether by ultrasound or other means, can result in evaporation of the liquid and formation of small bubbles[35]. These bubbles can act as nuclei for the previously described bubble cavitation, however, the pressure required for their formation is relatively high (e.g., the pressure required to evaporate water at room temperature is on the order of 10^5 Pa)[36].

3.4 Microbubbles

Microbubbles (MBs) are gas-filled shells of micrometric diameter, originally developed for US imaging due to their strong echogenicity[37]. Over the years MBs formulations were improved to yield uniformly sized bubbles that can be injected into a patient's blood stream,

these MBs are small and elastic enough to be carried through small capillaries and reach multiple target organs[38].

As discussed in the section 3.3, sonication of a gaseous bubble within a liquid can yield different outcomes depending on the frequency and amplitude of the driving pressure. however, in the case of shelled MBs, some of the assumptions made before no longer stand, mainly- their small size and coating enhance the effect of surface tension, moreover, the MB shell imposes limitations on the bubble radius as it may rapture when the bubble size is significantly increased or buckle when the bubble is significantly compressed (Figure 3).

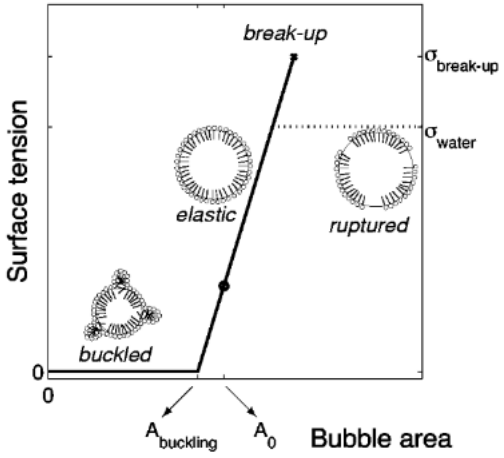

Figure 3: The MB area can only remain within a certain range. The lower limit is imposed by buckling of the bubble shell whereas the upper limit represents shell rapture. Adopted from Marmottant et al. (2005)[39]

These changes were incorporated into the RPE by Marmottant et al.[39] that formulated the following model for a gas filled MB with a lipid monolayer coating:

$$\rho\left(\ddot{R}R+\frac{3\dot{R}^2}{2}\right)= \tag{10}$$

$$\left[P_0+\frac{2\sigma(R)}{R_0}\right]\left(\frac{R_0}{R}\right)^{3\kappa}\left(1-\frac{3\kappa}{c}\dot{R}\right)-P_0-\frac{2\sigma(R)}{R}-\frac{4\nu_L\dot{R}}{R}-\frac{4\kappa_s\dot{R}}{R^2}-P_{ac}(t)$$

Here, c is the speed of sound in the liquid, and the driving pressure is composed of a slow changing ambient pressure P_0 and an alternating component $P_{ac}(t)$. The surface dilatational viscosity of the lipid monolayer κ_s is a function of the lipid layer thickness and its viscosity.

Note that in this equation the surface tension σ is a function of the radius, and is explicitly formulated:

$$\sigma(R) = \begin{cases} 0 & if\ R \leq R_{buckling} \\ \chi\left(\frac{R^2}{R_{buckling}^2} - 1\right) & if\ R_{buckling} \leq R \leq R_{break-up} \\ \sigma_{water} & if\ R_{break-up} \leq R \end{cases} \quad (11)$$

In (11), the first case describes buckling of the shell, and the last case represents bubble collapse due to shell rapture, where the measured surface tension will be equal to the surface tension of water σ_{water}. The buckling radius, $R_{buckling}$ may be explicitly calculated if the number of lipid molecules that form the shell, and the area of a single lipid molecule are known. χ is the elastic compression modulus which can be empirically measured.

Due to their cavitational properties, MBs offer a unique therapeutic tool that can be utilized in a variety of mechanisms. The first therapeutic use cases of MBs were as vehicles for targeted drug delivery[40], and as tools for penetration of biological barriers, such as vessel walls[41] and cell membranes[42]. These, alongside other therapeutic procedures, utilized the mechanism of inertial cavitation.

3.5 FUS-mediated BBBD

As the use of FUS for brain treatment gained interest, evidence of the physiological effects of FUS on the brain started to surface. One of the more interesting observations was that insonation of the brain with appropriate US parameters may induce nonlethal functional changes, among which is a localized BBB disruption (BBBD)[43]. Only three decades later, was this phenomenon linked to the occurrence of acoustic cavitation[44], which eventually led to the development of a controlled mechanism for local and reversible BBBD, that utilizes IV-injected MBs and FUS[45].

In FUS-mediated BBBD, MBs are injected into the vascular system and a FUS beam is directed to a specific brain region, this causes the bubbles within the US focus to stably

cavitate. While cavitating, the MBs exert force on the endothelial cells of the vessel walls, thus activating multiple cellular mechanisms[46] that increase the BBB permeability and allows substances within the vascular system to perfuse into the parenchyma[2].

3.5.1 In-situ monitoring of MB cavitation

As previously discussed, stable cavitation of MBs within a brain blood vessel may lead to safe and transient BBB opening. However, if the sonication peak-negative-pressure (PNP) is increased enough to cause inertial cavitation of the bubbles, the shockwave emitted upon MB collapse may lead to microhemorrhages and tissue damage[47,48]. Therefore, safe BBBD requires careful selection of the PNP to maintain the MBs in stable cavitation. Fortunately, both theoretical models and experimental measurements show that the two modes of MB cavitation, namely stable and inertial, may be distinguished by specific acoustic emissions[49,50]. While stable cavitation is characterized by acoustic echoes at the sonication frequency as well as its harmonies, inertial cavitation is characterized by a broadband emission.

The acoustic echoes from insonated bubbles may be monitored in real time by passive recording using an ultrasound transducer. The recorded radiofrequency (RF) signal undergoes real-time fast-Fourier-transform (FFT) to visualize the signal spectral content. This method is known as passive cavitation detection (PCD), and is often used as live feedback for safe FUS-mediated BBBD[51].

More recently, two empirical measures for PCD were introduced, which are stable cavitation dose (SCD) and inertial cavitation dose (ICD). The process of extraction for these measures is described in detail in the Methods section. ICD and SCD can be used together to determine the safety and effectivity of FUS-mediated BBBD in real-time[52].

3.6 Proposed method concept

Here, we present a method to characterize the perfusion of fluorescent molecules from the vascular system into the parenchyma following FUS-mediated BBBD. EB leakage was used as marker for BBBD, whereas blood vessels localization was done using FITC labeled Dextran. Automated image processing pipeline was developed to quantify the extent of extravasation as function of microvasculature diameter at a single blood vessel resolution, together with a wide range of additional parameters, including blood vessel diameter distribution, blood vessel length and bifurcation density for each brain region, and the fraction blood vessels that exhibit strong BBB.

4 Materials and methods

4.1 Microbubble preparation

MBs were prepared and measured as described in previous studies[19,53]. The MBs were composed of a phospholipid shell and a perfluorobutane (C4F10) gas core. The lipids (2.5 mg per 1mL) were Distearoylphosphatidylcholine (DSPC; 850365C) and 1,2-distearoyl-sn-glycero-3-phosphoethanolamine-N-[methoxy(polyethylene glycol)-2000] (ammonium salt) (DSPE-PEG2K; 880129C) (Sigma Aldrich, St Louis, MO, USA) were combined at a molar ratio of 90:10 and made using a thin film hydration method. A buffer (mixture of glycerol (10%), propylene glycol (10%) and saline (80%) (pH 7.4)) was added to the lipids and sonicated at 62°C. The MB precursor solution was aliquoted into vials with liquid volume of 1 mL and saturated with perfluorobutane. Prior to their use, the vials were shaken for 45 sec in a vial shaker and purified via centrifugation to remove MBs smaller than 0.5 µm in radii. Size selection was applied as described previously to remove MBs larger than 5 µm in diameter. The size and concentration of the MBs was measured with a particle counter system

(AccuSizer® FX-Nano, Particle Sizing Systems, Entegris, MA, USA). The bubbles were used within three hours of their preparation. The size distribution and concentration varied by less than 10% between the measurements.

4.2 Passive cavitation detection in blood vessel mimicking tubes

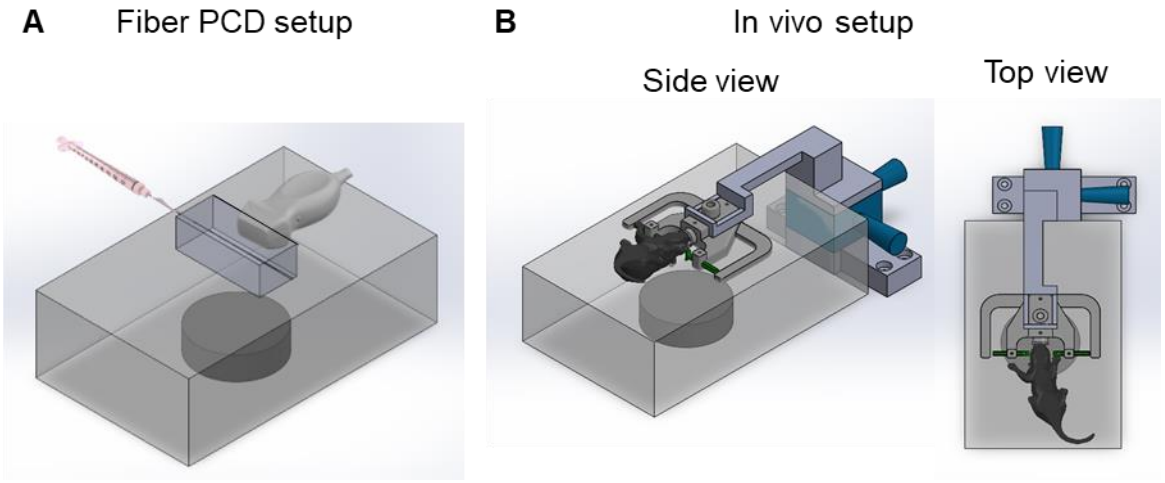

Figure 4 : Experimental setups. (A) In-vitro, a 250 kHz single element transducer was used to insonify tissue-mimicking phantom embedding tubes of either 280 or 100 µm with a MB suspension. PCD was performed with an array transducer located perpendicularly to the therapeutic transducer. The acoustic echoes were processed, yielding results as a function of the applied PNP and the different tube diameters. (B) In-vivo setup. The mouse was mechanically positioned at the focal spot of an US transducer, located at the bottom of a water tank, using a custom holder.

The US setup (Illustrated in Figure 4A) was composed of a spherical single element FUS transducer (H115, Sonic Concepts, Bothell, WA, USA), operating at 250 kHz center frequency, with a focal distance of 45 mm, and an aperture diameter of 64 mm. The transducer was located at the bottom of a water tank, facing upwards. This transducer was operated either by a function generator (AFG1012, Tektronix Inc., Beaverton, OR USA) and a RF amplifier (2100L, Electronics & Innovation, Ltd., Rochester, NY, USA) for the fiber experiments, or a transducer power output system (TPO-200, Sonic Concepts, Bothell, WA, USA) for the in-vivo experiments. The PNP at the focal spot was calibrated using a needle hydrophone (NH0500, Precision Acoustics, UK). Pure agarose phantom embedding blood vessel mimicking tubes were placed at the transducer focal spot. These agarose phantoms

were prepared by mixing 1.5% agarose powder (A10752, Alfa Caesar, MA, USA) and deionized water. The solution was heated until all the powder had completely dissolved, and then was poured into a custom laser-cut mold. The mold measured 65 mm × 29 mm × 25 mm (length x width x height) and contained a hole in the parallel sides to insert the tubes. The PTFE tubes had inner diameters of either 280 µm (BTPE-10, Instech laboratories Inc., Plymouth meeting, PA, USA), or 100 µm (PTFE Extruded Sub-Lite-Wall® Zeus, Orangeburg, SC, USA). Since the liquid volume, and hence the quantity of MBs was larger within the 280 µm tubes, three 100 µm tubes were connected in parallel to increase the total cross-section. An imaging phased array transducer (ATL P4-1, Philips, Seattle, WA, USA) was placed perpendicularly to the agarose phantom, and to the FUS transducer, and was aligned to focus on the tube. This transducer was controlled by a programmable US system (Verasonics, Vantage 256, Verasonics Inc., Redmond, WA, USA), that was used for conducing PCD.

A diluted MB solution was injected into the tube phantom. To match the MB concentration to a similar concentration as used in mice models[19], the MB solution was diluted with degassed Dulbecco's phosphate buffered saline (PBS; 02-023-1A, Biological Industries Israel, Beit-Haemek, Israel) to a final concentration of 12.5 [ml^{-1}]. The function generator was triggered by the Verasonics system and transmitted a single sinusoidal burst of 100 cycles at a center frequency of 250 kHz. During sonication, the PCD array recorded for 1.6 seconds. This injection-transmit-receive sequence was repeated with different sonication PNPs, and the tube was flushed with PBS between measurements. For controls, the same sequence was performed while PBS was injected instead of diluted MB solution.

4.2.1 Passive cavitation detection data analysis

The acquired RF signals from each transducer element were applied with a fast Fourier transform, and the frequency-domain signals were averaged to enhance the signal-to-noise-

ratio. SCD and ICD were extracted according to the method presented in Farny et al.[54]. Briefly, a high-pass-filter with a cutoff frequency of 1.5 x f0 was then applied to eliminate the contribution of the transmitted wave. Next, a 20 kHz window was defined around each harmonic of the transmission frequency (a harmonic is defined as n x f0, n=1,2,3…). A modified comb filter was applied to eliminate the peaks in these windows and replace them with random samples from the conjugated regions of the spectrum. The ICD was defined as the root-mean-squared (RMS) amplitude of the filtered signal. The SCD was calculated as the difference between the RMS of the original signal after HPF and the ICD. Finally, the results of SCD and ICD were normalized by the vessel cross-section to compensate for a possible decrease in MB quantity caused by the liquid volume as in the 100 µm tubes.

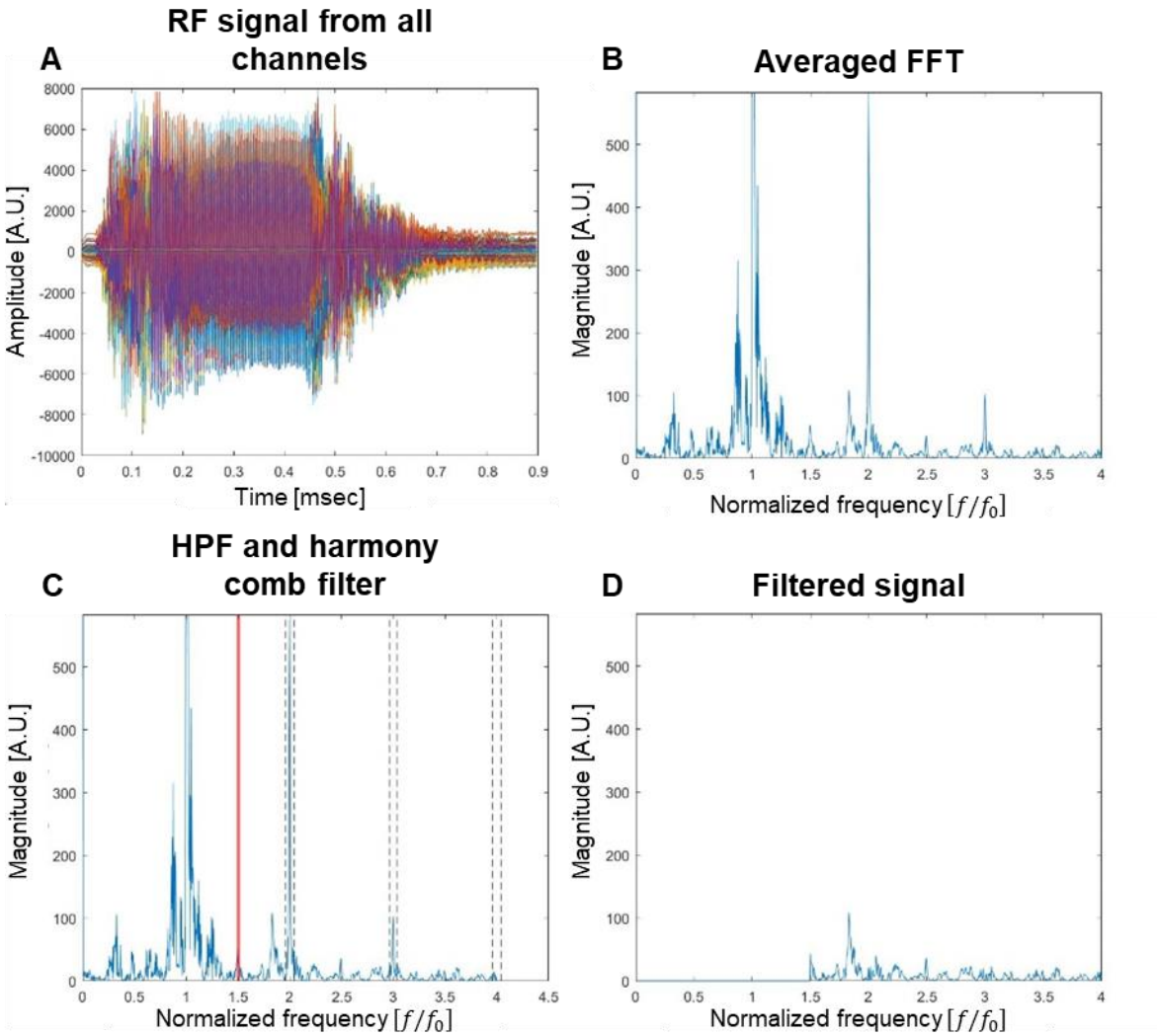

Figure 5: PCD signal processing. The original RF signal is recorded simultaneously in all of the array elements (A). Each of the signals undergoes FFT and the Fourier transforms are averaged to eliminate noise (B). a HPF with a cutoff frequency of $1.5 \cdot f_0$ is applied to eradicate the contribution of the transmission signal. A custom comb filter is used to remove the power in spectral windows surrounding the full harmonies of the transmission frequency, windows are marked by the dashed lines and the cutoff frequency is marked by the solid red line (C). The filtered signal represents only the contribution of the broadband emission (D). The ICD is computed as the RMS of the signal in (D) whereas the SCD is computed as the difference between the RMS of the signal after HPF and the ICD.

4.3 In-vivo BBBD

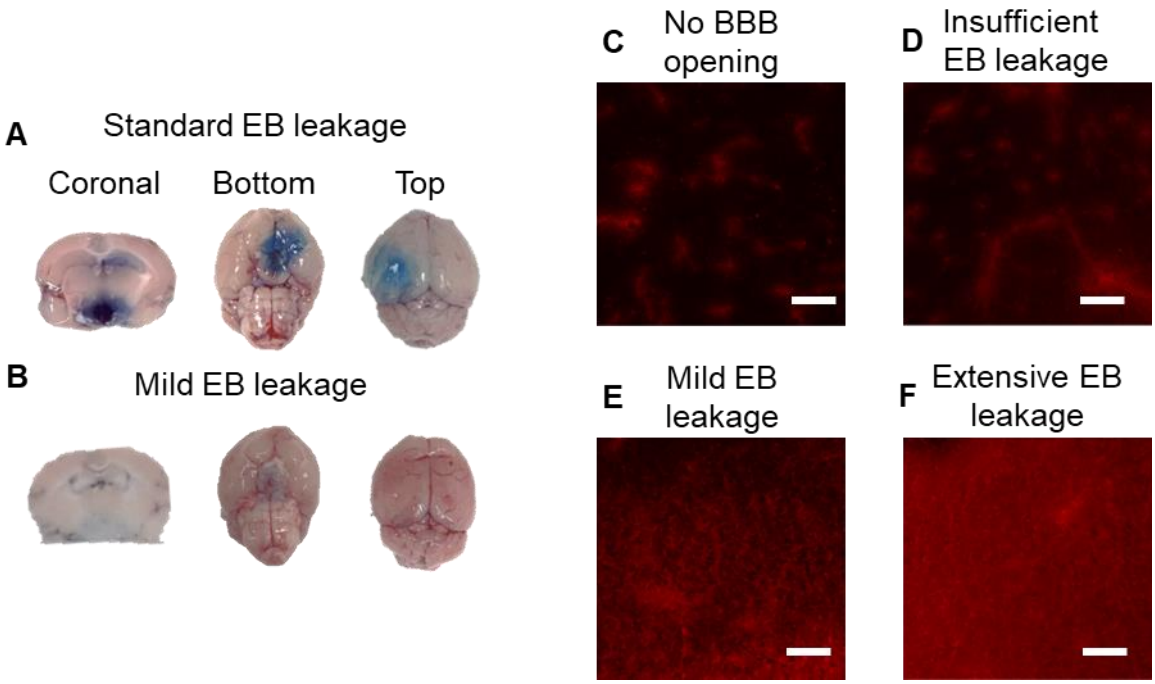

Figure 6: Evans blue extravasation following US-mediated BBBD. (A) Standard EB leakage in treated brains, showing bright blue spots where BBBD was performed. (B) Mild EB leakage in treated brains required for localizing BBBD at the resolution of a single blood vessel. Fluorescence microscopy images of EB leakage for: (C) No BBBD. (D) Insufficient EB leakage. (E) Mild EB leakage. (F) Extensive EB leakage. (C) -(F) 50 µm scale bars.

A total of 102 mice were used in the in-vivo experiments. Female C57BL/6 mice (10-11 weeks old, 16-21g, Envigo, Jerusalem, Israel) were used in the in-vivo experiments. The mice were anesthetized with 1.5% isoflurane using a low flow vaporizer system (50 ml/min, SomnoFlo, Kent Scientific). The mice heads were completely shaved, and US gel was applied. The mice were placed in a supine position on top of an agarose pad, at the focal spot of the FUS setup described in the PCD experiments section. The mice were mechanically aligned using a custom two-axis (X-Y) stereotaxic system that was connected to the water tank (Figure 4B). The focal spot size was 7 mm laterally and 50 mm axially, which is appropriate to conduct BBBD in large brain portions, and mainly in the hypothalamus. BBBD was performed by systemically injecting 2 x 107 MB in 50 µl of degassed PBS. Thirty seconds post MB injection, the mice received the FUS treatment consisting of 1 ms bursts at 250 kHz. The total sonication period was 60 seconds with a PRF of 1 Hz (0.1% duty-cycle).

Sonication PNP was optimized to induce safe, mild BBBD, that was visible in fluorescent microscopy, without signs of microhemorrhage in histology. The selected PNP was 263 kPa (a driving power of 2.5 W with the TPO system). After sonication, the mice were systemically injected with two dyes: 2% Evans Blue dye (EB; E2129, Sigma Aldrich) (4 ml/kg, diluted in PBS), and 6 mg/ml Fluorescein isothiocyanate–Dextran (FITC-Dextran; 46946, Merck, Kenilworth, NJ, USA) (4 ml/kg, diluted in normal saline). Three different EB circulation times were tested: 8, 18, and 28 minutes, to identify the optimal circulation duration that enabled localized EB detection for each blood vessel (Figure 7).

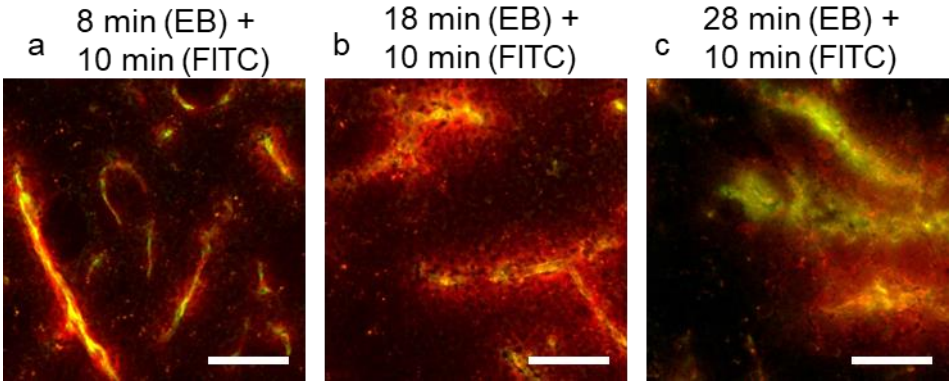

Figure 7: Optimization of EB circulation times. Microscopy images of brains that underwent BBB opening, after a 10 min circulation time of FITC-dextran, and EB circulation times of (a) 8 minutes, resulting in insufficient leakage upon BBB opening. (b) 18 minutes that yielded the best results for leakage localization and (c) 28 minutes that resulted in widespread EB leakage that impeded leakage source localization. 50 μm scale bars.

FITC-Dextran circulation time was 10 minutes to maintain a strong fluorescence signal inside the vessels, without leakage[16]. In between injections, the mice were anesthetized, and allowed to wake up for better circulation. Two groups of mice were tested in each experiment: a no treatment control group that was injected with the two dyes but did not receive MB + FUS treatment, and a treated group with MB + FUS and the dyes .

Ten minutes post FITC-Dextran injection, the mice were euthanized and decapitated. The brains were quickly harvested, covered in tissue freezing medium (Leica OCT cryocompound, Leica Biosystems, Nussloch GmbH, Heidelberger, Germany) and flash-frozen using liquid nitrogen. After flash-freezing, the brains were transferred to a -80ºC

refrigerator. The freezing procedure was established by comparison to standard Paraformaldehyde (PFA; 50-259-99, Merck). Fixation was done by placing the fresh tissue in 4% PFA solution for 24 hours, then transferring to 30% sucrose solution up to full precipitation, after which the brains were washed with PBS, frozen with liquid nitrogen and transferred to -800C for storage. The PFA preservation resulted in the leaking of the FITC-Dextran outside the vascular system and did not allow for vessel segmentation.

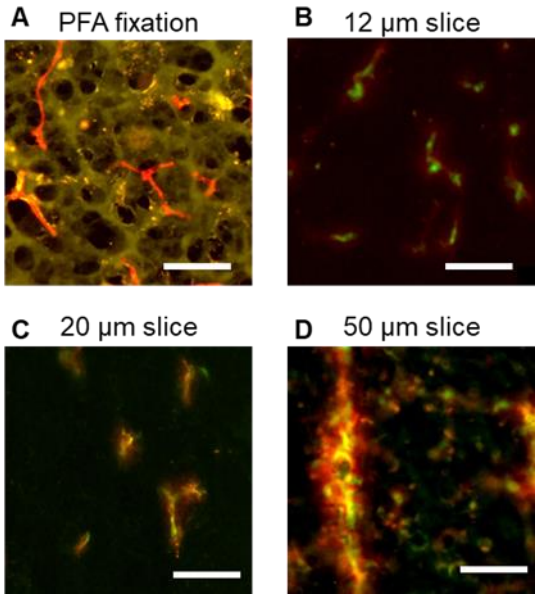

Figure 8: Brain preservation and slice thickness optimization of the control brains. Microscopy images of (A) PFA fixed brain, and flash frozen brains with slice thickness of (B) 12 µm. (C) 20 µm. (D) 50 µm. Scale bars are 50 µm.

4.3.1 Microscopy imaging

On the day of microscopy imaging, the frozen brains were transferred to a -20ºC cryostat microtome (CM1950, Leica Biosystems) and coronally cut to slices of different thicknesses. The sections were placed on standard microscope slides within a closed slide box for air-drying at room temperature for 5 - 60 minutes. Three different slide thicknesses of 12, 20 or 50 µm were tested for the non-treated control brains, to optimize the number of clearly visible blood vessels with a good signal and reduced blurriness that can be a byproduct of out of focus planes (Figure 8). The optimal thickness of 20 µm was selected for the treated brains and the PFA preserved brains. The brain slides were imaged within 1 hour of sectioning to

avoid further EB perfusion[16]. Images were acquired with a motorized upright fluorescence microscope (BX63, Olympus, Tokyo, Japan) with a x20 objective (UPLFLN 20X, Olympus). This objective had a focal depth of 1.1 µm. The excitation wavelengths and exposure times were 508 nm and 1150 msec for FITC-Dextran, and 615 nm and 115 msec for EB. All the imaging parameters were consistent for all sections. The final images were 1920 x 1200 pixels in size, with a pixel size of 0.29 µm in the imaging plane.

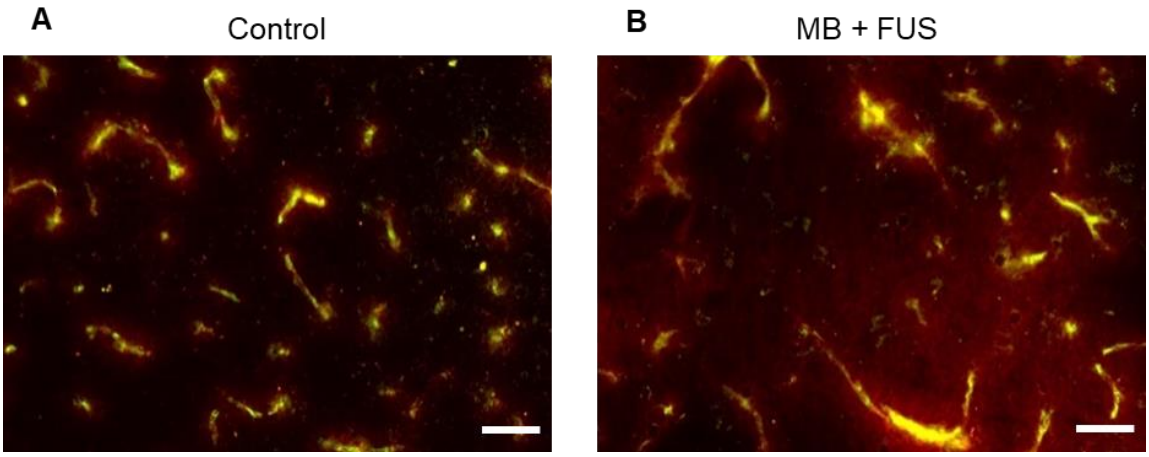

Figure 9: Microscopy images of brain slices. Blood vessels appear in green, while extravasated EB is red. (A) Control brain without BBBD, where the green and red channels overlap. (B) MB+FUS treated brain demonstrating EB extravasation to the perivascular area. Scale bars are 50 µm.

4.3.2 Image processing

Microscopy image processing was performed using MATLAB. Preprocessing included the splitting of all images into two channels: the green channel that marked the blood vessels with FITC-Dextran and the red channel that showed EB extravasation from the blood stream into the surrounding perivascular area. Post processing was then applied as follows. The first step utilized the green channel to perform blood-vessel segmentation and characterization. This was carried out using a modified version of the Rapid Editable Analysis of Vessel Elements Routine (REAVER) tool[55], that was adjusted specifically for this task. Segmentation yielded a binary mask of all vessels in the frame, from which the vascular skeleton was extracted (Figure 10D). Branchpoint localization was used to separate the vascular network into individual vessels, which were then used for BBB leakage quantification.

The second step was to calculate the single vessel median radius as described by Corliss et al.[55]. Briefly, for each point on the vessel centerline, the distance to the closest point outside the vessel was calculated. This distance represented the local vessel radius. The median of all local radii of the vessel was calculated. Two other network morphology features were extracted for each frame: the bifurcation density and the length density. The bifurcation density was calculated as the number of bifurcations in the vascular skeleton divided by the frame area, and the length density was calculated as the total length of the vessels divided by the frame area.

After obtaining the morphological features of the blood vessels, the following steps were carried to quantify EB extravasation and BBBD for each blood vessel. In the third step, the binary mask obtained from the green channel was applied to the red channel. By doing so, the interior of each blood vessel was removed from the frame, leaving behind a frame with the EB intensity in the perivascular area (Figure 10E). This step served to remove the blood vessel content itself and focus on the EB extravasation.

In the fourth step, the size of the perivascular area around the blood vessels was determined. This area was defined by two user specified constants: the initial distance from the vessel wall (W_i) which was used to eliminate segmentation-related errors, and the perivascular area width (d). Then, individual blood vessels were extracted from each image by subtracting the entire vascular mask from the single-vessel perivascular area mask. This was done to make sure that the perivascular area did not include nearby vessels.

In the final step, the EB channel intensity was rescaled to a range of [0,1] and the median pixel intensity in the perivascular area (defined in the previous steps) was calculated. Steps 3-5 were repeated for each blood vessel in each frame.

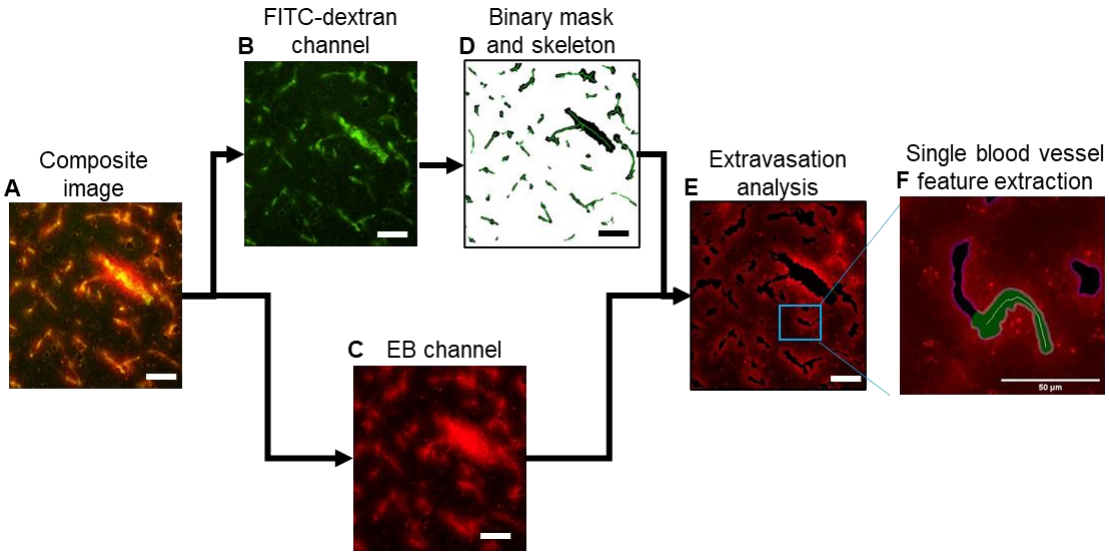

Figure 10: Image processing scheme. (a) The original composite image was split two channels: (b) The green (FITC-Dextran) channel marking the blood vessels, and (c) the red, EB channel. (d) Morphological operations were applied (b) to perform vessel segmentation and skeleton extraction. (e) The binary mask in (d) was applied to the EB channel in (c). (f) The resulting image was used to determine the EB intensity in the perivascular ROI surrounding each vessel, and the vessel skeleton was used to extract the morphological features of each vessel. Finally, the median pixel intensity was quantified as a function of blood vessel diameter for the entire microvasculature population. Scale bars are 50 µm in all subfigures.

4.3.3 Quantitative analysis

Vascular morphology in different regions of the brain (hippocampus, hypothalamus, striatum, and thalamus) for the control and MB + FUS treated groups was evaluated by quantification of length and bifurcation density (Figure 12C, D). The microvasculature diameter distribution was calculated and plotted as a diameter histogram (Figure 12A, B). Since the majority of the blood vessels in the mouse brains were smaller than 10 µm (average diameter was 4.98 ± 1.9 µm), we chose to exclude large vessels (with diameters exceeding 10 µm, based on previous studies[56,57]), and vessels with unclear borderlines.

In the second stage, EB quantification was performed for individual blood vessels, where in bifurcating vessels the segments before and after the bifurcation were considered two separate blood vessels. Different perivascular areas were compared. Three initial distances from the blood vessel wall, W_i, of 0, 2 and 5 pixels (corresponding to 0, 0.59 and 1.46 µm), and three different perivascular widths, d, of 1, 5, and 10 pixels (0.29, 1.46 and

2.93 μm). For each combination of hyperparameters, the EB intensity results were divided into groups based on the vessel diameter. Vessels with diameters of 2 – 10 μm were sorted into diameter groups at 1 μm intervals (2-3, 3-4, …,9-10 μm). The EB intensity in the perivascular area was calculated for each blood vessel in each diameter group, for the control and treated brains, and plotted as EB intensity histograms (Figure 13B, C), and as a comparison to other diameters (Figure 13D, E). Note that each frame contained blood vessels with different orientations, ranging from circular cross sections when the blood vessels were perpendicular to the image plane, to lines when they were parallel to the imaged plane. To reduce segmentation noise in the small capillaries (<4 μm), blood vessels with a minimal length of less than 10 μm were removed. The number of capillaries that were used for the analysis was 1075.

Finally, the percentage of BBBD blood vessels for each diameter group was assessed by setting a threshold that was determined based on the EB intensity of the control group for each diameter. The threshold was two standard deviations above the mean control EB intensity. In the treated group, and for each diameter, all the blood vessels whose EB intensity exceeded the corresponding threshold were considered a strong BBBD (Figure 13E). This analysis was conducted for each frame and vessel diameter. Comparisons were carried out between frames.

4.3.4 Hematoxylin and Eosin staining

The safety of the BBBD treatments was assessed with standard Hematoxylin (3801542, Leica Biosystems) and Eosin (3801602, Leica Biosystems) staining of the sliced brain sections. The stained slides were imaged using the brightfield channel of the same microscope as for fluorescence imaging.

4.4 Statistical analysis

Statistical analysis was performed using MATLAB and GraphPad Prism. The results are presented as the mean ± SD. Statistical tests are reported in the t captions. P values of less than 0.05 were considered significant and were adjusted for multiple comparisons as indicated in the captions.

5 Results

5.1 Passive cavitation detection

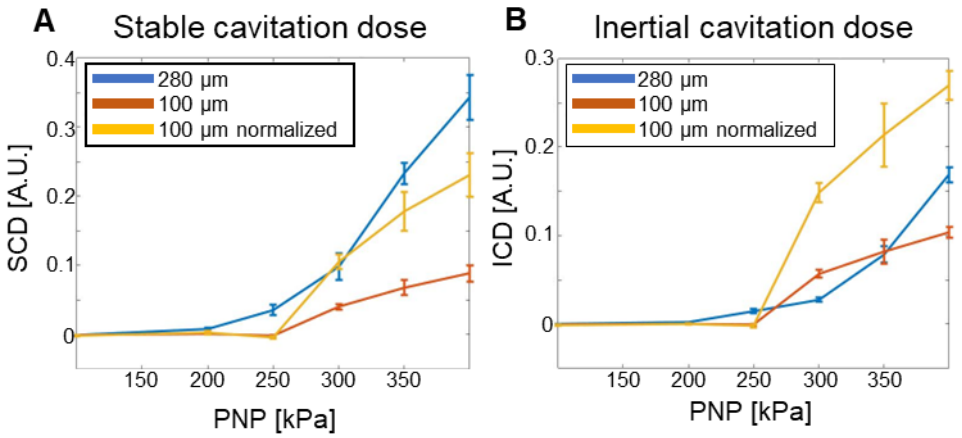

Figure 11 : Quantitative measures extracted from passive cavitation detection in blood vessel mimicking tubes. (A) SCD, and (B) ICD. (A), (B), 280 µm and 100 µm results are depicted by the blue and orange lines, respectively. The yellow line represents the results of the 100 µm capillary when multiplied by the cross-section ratio.

MB oscillations were evaluated in blood vessel mimicking tubes via PCD, to identify variations as a function of tube diameter. PCD was performed with an imaging array, upon MBs interaction with a therapeutic pulse at a center frequency of 250 kHz (Figure 4A). The SCD and ICD were computed based on the recorded RF echoes[52]. Both SCD and ICD increased as a function of the applied PNP; however, the onset of the SCD increase occurred at a PNP of 200 kPa for the larger tube with a diameter of 280 µm, and a PNP of 250 kPa for the smaller 100 µm tube (both for the raw data and the normalized data based on MB volume

within the tube) (Figure 11A). The onset of ICD shifted similarly to the SCD; however, the increase slope was steeper for the 100 µm normalized fiber (Figure 11B). This suggests that there was a sharp transition between stable and inertial cavitation for MBs in smaller tubes.

5.2 In-vivo experiments

BBB extravasation as a function of blood vessel diameter was assessed in-vivo. Mice underwent BBBD using MB and 250 kHz US. Subsequently, two fluorescent dyes were systemically injected: 2000 FITC-Dextran that fluoresces in green and stains the blood vessels, and EB that fluoresces in red and serves to evaluate the BBB extravasation. In the first set of experiments, the brain preservation and microscopy imaging techniques were optimized to determine the brain slice thickness, microscope parameters and the dye circulation durations prior to brain harvesting. The optimized parameters were then used to quantify BBBD.

5.2.1 Optimization experiments

Two brain preservation methods were tested on control mice (no BBB-opening), either using standard PFA fixation or flash-freezing using liquid-nitrogen (Figure 8). After PFA fixation, there was FITC-Dextran leakage from the blood vessels that made it impossible to localize the blood vessels (Figure 8A). In comparison, blood vessels were easily identified in the green channel using the flash-freezing technique which was hence selected for the subsequent experiments. The next step was to choose the slice thickness using the control brains. The 12 µm slices yielded blurry images with heterogeneous coloring within the blood vessels, whereas the 50 µm slices were blurry due to out-of-focus blood vessels beyond the depth of field. The 20 µm slices yielded the highest quality images, with a clear view of the blood vessels, and an overlap between the green and red channels (Figure 8B-D).

Next, BBBD was performed using a custom setup (illustrated in Figure 4B). Standard EB leakage following BBBD resulted in blue stains that were visible in the brain (Figure 6A). However, these strong stains implied broad extravasation and perfusion of the EB within the brain tissue that prevented blood vessel localization. Here, to enable BBBD detection at the resolution of a single blood vessel, mild EB leakage was required (Figure 6B). Fluorescent images of the EB leakage pattern can also be used to optimize EB extravasation (Figure 6C-F). This amount of extravasation was achieved by adapting the EB circulation duration. This was done to identify a duration that was long enough to allow EB perfusion into the parenchyma following BBBD, while avoiding widespread diffusion that would make the leakage source undetectable (Figure 7). The FITC-Dextran circulation duration was 10 minutes, based on previous studies[16]. This duration was selected as a tradeoff between effective vascular staining and minimized possible BBB penetration, since larger molecules require a longer circulation time to extravasate from the blood stream. The sonication pressure was chosen such that no signs of microhemorrhage were observed during histology (PNP of 263 kPa).

5.2.2 Single blood-vessel-based BBB opening quantification

Microscopy images of brain slices following BBBD with US and MBs showed reliable blood vessel staining (green) and widespread extravasation of EB (red) around the blood vessels compared to the control brains. In the control brains, the EB was confined to the blood vessels and thus overlapped with the green channel (Figure 9A). In the treated brains, variations in EB intensity around each blood vessel were visible (Figure 9B).

Quantification of the amount of EB extravasation was carried out by an automated image processing algorithm developed for this task, which is discussed in the Materials and Methods section (Figure 10). Briefly, the original image was split into two channels. The green channel was used for vessel segmentation and morphological feature extraction (Figure

10B, C). The red channel was used to quantify EB intensity around each blood vessel (Figure 10D). The median pixel intensity of the normalized red channel was calculated in the region of interest (ROI) chosen according to the processing of the green channel. Extravasation was then analyzed for each blood vessel individually, resulting in a detailed quantification of a range of parameters, including blood vessel diameter distribution, blood vessel length and bifurcation density for each brain region, amount of EB extravasation as a function of blood vessel diameter, and the fraction of strong BBB opened blood vessels.

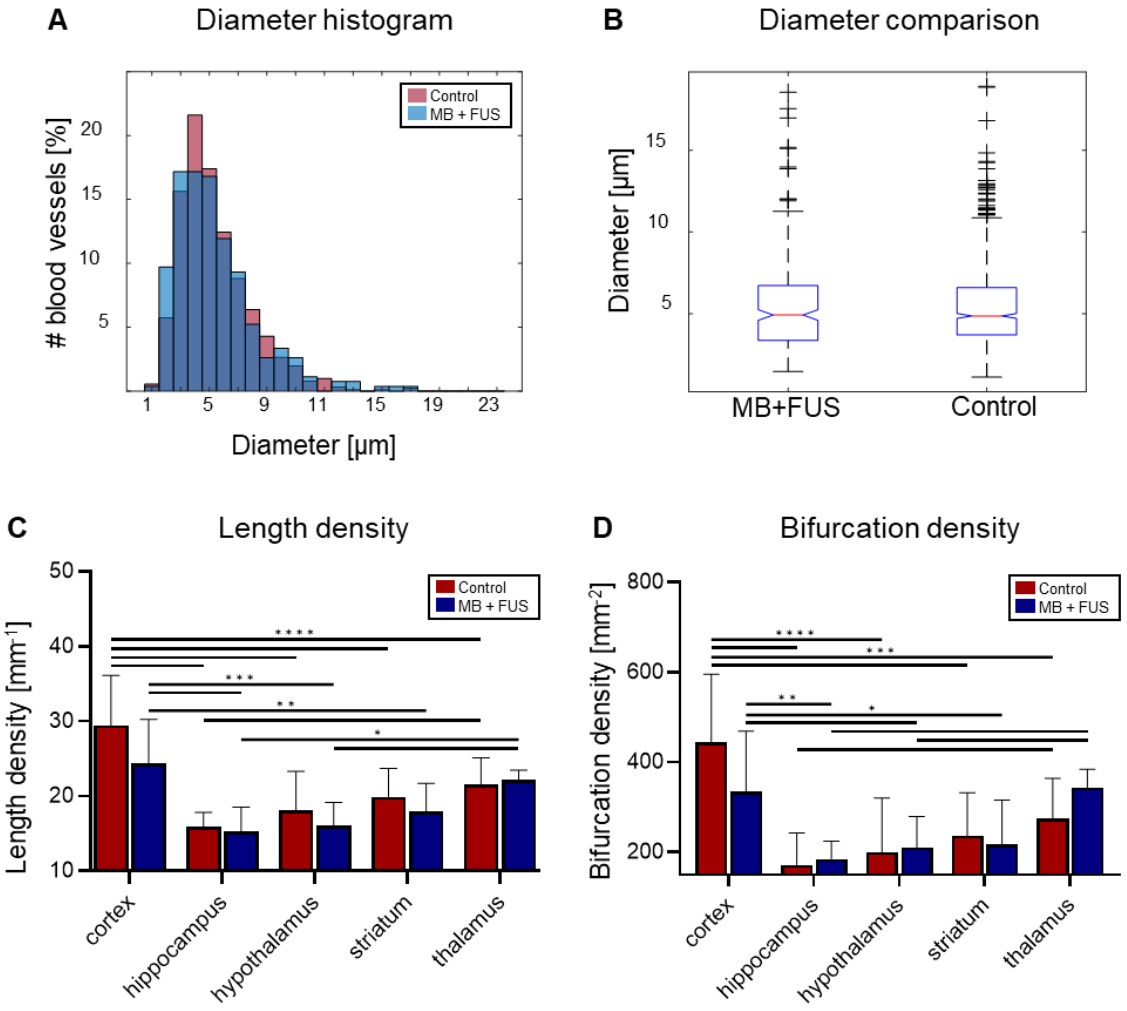

Figure 12: Blood vessel morphological characterization. (A) Microvasculature diameter histogram for the control and MB + FUS treated brains. (B) Diameter comparison analysis for (A), Welch's t-test revealed no significant differences (total of n = 908 and n = 268 blood vessels for the control and MB + FUS groups, respectively). Vessel density analysis in different brain regions, (C) length density, (D) bifurcation density (total of n = 45 and n = 39 frames for the control and MB + FUS groups, respectively), Fisher's LSD test. The p values were *p<0.05, **p<0.01, ***p <0.001, ****p <0.0001. All data are plotted as the mean ± SD.

The image processing algorithm was initially applied to both the control and the treated datasets to compute the microvasculature diameter distribution within the regions where the BBB was opened. The average microvasculature diameter was 4.98 ± 1.9 μm and was similar in the control and treated groups ($p>0.05$, non-significant). This diameter distribution is consistent with previous reports of cerebral capillary diameters in mice[57,58]. The vasculature density and length were also evaluated using the algorithm. Comparing these parameters for different brain areas revealed a significant increase in vascular density, in terms of length and bifurcation density in the cerebral cortex as compared to more ventral parts of the brain (hippocampus, hypothalamus, striatum, and thalamus) which is congruent with previous reports[11] (Figure 12C, D). No significant differences were found between the control and treated groups.

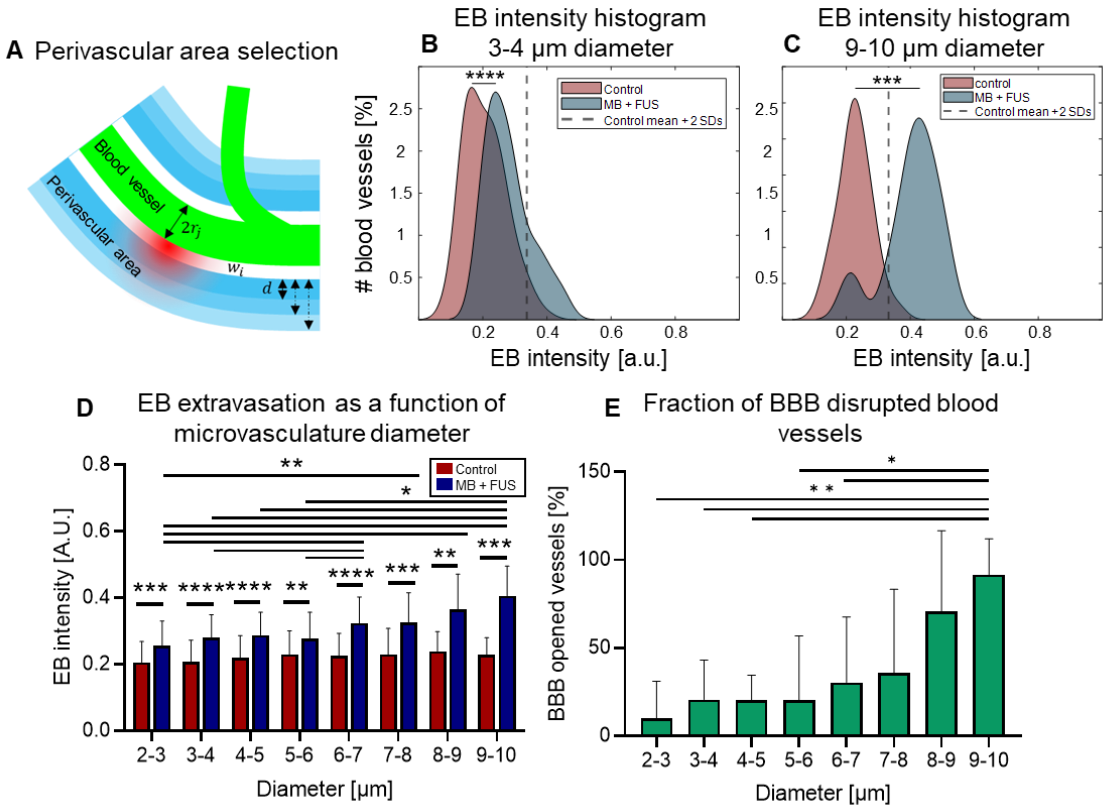

Figure 13: EB extravasation quantification as a function of blood vessel diameter. (A) The perivascular area around each blood vessel with a diameter of $2r_j$ was defined by its initial distance from the vessel wall (W_i) and total width (d). In each diameter group, the EB intensity in the perivascular area was calculated. The EB intensity histogram for blood vessels with diameters of (B) 3-4 µm, and (C) 8-9 µm. Welch's t-test. (D) EB extravasation as a function of microvasculature diameter. (E) Fraction of strong BBBD blood vessels. (D, E) Mixed-effect model with Geisser-Greenhouse correction and the two-step step-up method for FDR control. The p values were *p<0.05, **p<0.01, ***p <0.001, ****p <0.0001. All data are plotted as mean ± SD.

Next, the EB intensity in the perivascular area surrounding individual blood vessels was extracted and compared across diameter groups for different perivascular area parameters (Figure 13A). A comparison of the EB intensity histograms in a perivascular area of 10 pixels (2.9 µm width), for 3-4 and 9-10 µm blood vessels (Figure 13B, C), showed increased levels of EB intensity in the MB + FUS treated brains compared to the control brains ($p<0.01$). In the control brains, a similar average EB intensity was observed for the two vessel diameters, whereas in the treated brains, EB intensity increased significantly for 9-10 µm blood vessels, compared to 3-4 µm ($p<0.05$). These findings were maintained when comparing blood vessels with diameters ranging from 2 to 10 µm (Figure 13D). The EB intensity in the control brains remained similar as a function of blood vessel diameter but increased significantly for the

treated brains (Figure 13D). In the treated brains, the EB intensity remained similar from 2 to 6 µm, but then started to increase with vasculature diameter. Changing the perivascular area parameters, such as the initial distance from the blood vessels used for the calculations, or the total distance from the blood vessel, did not significantly affect the results (Figure 14). For each blood vessel diameter histogram as shown in Figures 13B, C, the fraction of strong BBB opened blood vessels was calculated by setting a threshold based on a value of two standard deviations above the control mean for each diameter (95% confidence interval, dashed black line). The fraction of blood vessels in the MB + FUS treated group that exceeded this threshold was considered BBB opened. The percentage of strong BBBD increased from 9.75% for 2-3 µm blood vessels and to 91.67% for 9-10 µm (Figure 13E).

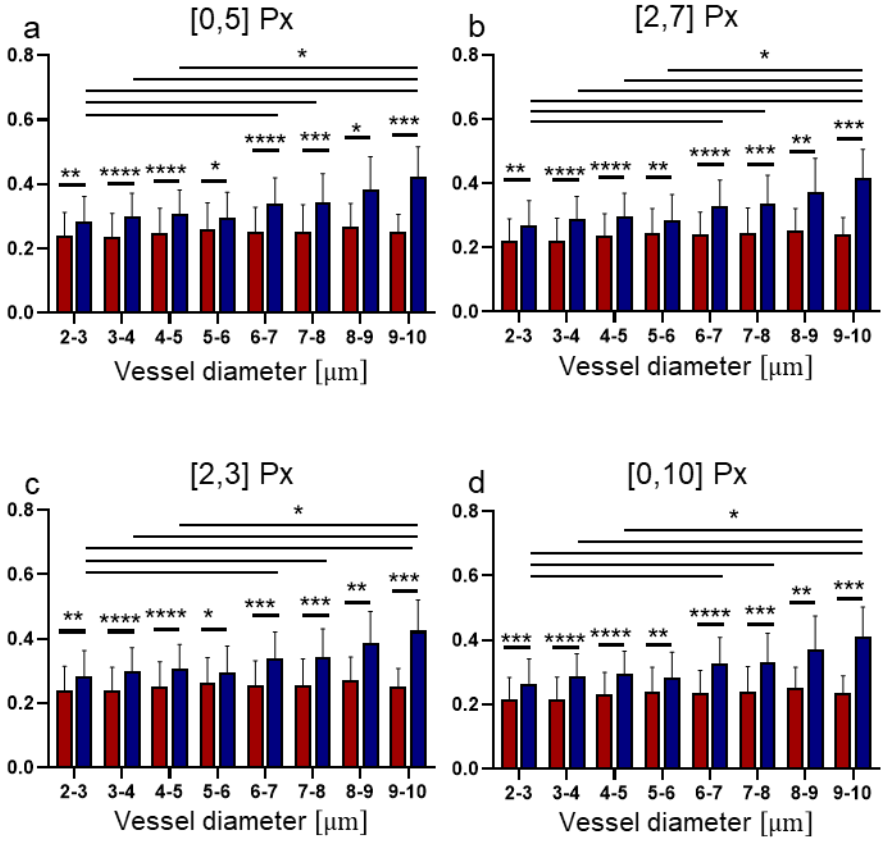

Figure 14: EB intensity in the perivascular area as function of diameter (red – control, blue – MB + FUS), for different choices of initial distance (W_i) and perivascular area width (d). (a) W_i = 0, d = 5 pixels (1.45 µm). (b) W_i = 2 pixels (0.59 µm), d = 5 pixels (1.45 µm). (c) W_i = 2 pixels (0.59 µm), d = 1 pixel (0.29 µm). (d) W_i = 0, d = 10 pixels (2.9 µm). Mixed-effect model with Geisser-Greenhouse correction and a two-step step-up method for FDR control. The p values were *p<0.05, **p<0.01, ***p <0.001, ****p <0.0001. All data are plotted as the mean ± SD.

6 Discussion

In this paper we present a method for quantitative evaluation of FUS-mediated BBBD at the resolution of the single vessel. The method involves the injection of two fluorescent dyes, at specific time points that are carefully designed for localized extravasation across the BBB. Microscopy imaging of brain slices and an automated image processing algorithm is then used to characterize brain capillaries based on diameter and morphology and assess the variation in BBBD as a function of blood vessel diameter. In order to label the blood vessels, the injection of a large MW green FITC-Dextran was used. Although large molecules, such as liposomes and cells[59,60], have been shown to cross the BBB following FUS-mediated BBBD, their diffusion times into the parenchyma are much longer. Here, mice were sacrificed 10 minutes post-injection, which suffices for efficient blood vessel staining by FITC-Dextran, without identified BBB penetration. Using fluorescence microscopy, the green FITC-Dextran channel was employed to segment the brain capillaries and extract their morphological features. The second dye was EB, which is a standard marker for blood vessel imaging[11] and is widely used for BBB opening identification and observation. Here, EB extravasation was probed for each individual blood vessel with and without FUS-mediated BBBD.

Applying the geometric blood vessel feature information, extracted from the green channel, to the red EB channel enabled us to quantify the diffusion of EB into the perivascular area surrounding each blood vessel. This method can quantify multiple parameters, such as the EB diffusion length, vascular density, vascular tortuosity, and microvasculature diameter. This is used to gauge EB intensity as a function of blood vessel diameter and compute the fraction of BBBD blood vessels. Our method is robust and can be used to gain important insights into unresolved questions related to FUS-mediated BBBD, such as the kinetics in capillaries with different diameters[61,62], the impact of vasculature diameter on BBBD properties such as the duration of opening, the ability to deliver molecules of different sizes

and their feasibility for brain drug delivery, and BBBD efficiency in different regions of the brain[63]. In addition, the method can facilitate the optimization of treatment parameters, such as bubble size, to improve the homogeneity of BBBD. Another future application of the method involves evaluating the effects of local microvasculature density on BBB opening. Studies have shown that microvascular density differs considerably between different brain regions and patients[64,65], which can lead to variations in BBB opening. Our platform is capable of assessing BBB openings at different regions while comparing the local vascular density, to identify variations.

Here, we focused on evaluating the effects of microvasculature diameter on the efficacy of BBBD. Variations in small blood vessels can be attributed to a combination of parameters. The first is reduced MB oscillations, that have been shown to be constrained in small tubes and blood vessels[7–9]. Another contributing parameter is the effective number of MBs. Although their concentration remains constant in the blood stream, given the smaller cross section of the capillaries, fewer MBs are present within these vessels compared to larger blood vessels. Similarly, smaller amounts of EB molecules flow within small capillaries, so that a gradual increase in EB intensity as a function of blood vessel diameter is expected; however, this was not the case for the results shown here, as EB extravasation remained almost constant for vessels smaller than 6 μm, and increased as function of diameter in larger vessels (Figure 13).

Single blood vessel extravasation following MB-mediated BBBD opening has been observed with two-photon fluorescence microscopy in mice[61,62,66,67]. Although this method provides high spatiotemporal resolution, our method has significant advantages. Our method can be applied to all brain regions, whereas two photon microscopy methods are limited by the laser penetration depth mainly to superficial regions such as the cerebral cortex. Furthermore, our method utilizes a fast, simple approach that does not involve complex in-

vivo procedures such as craniotomies, or unique experimental setups. It also enables the imaging and processing of large brain regions, which facilitate the characterization of large numbers of blood vessels simultaneously. In real-time two-photon microscopy, there is a tradeoff between spatial resolution, sensitivity, and acquisition time. As a result, the field of view is generally smaller. Finally, our approach provides a high resolution of 1 μm that can detect differences between vessels with a diameter of less than 10 μm, where large variations in BBB extravasation are observed. To scan a larger field of view, two-photon microscopy methods minimize scan duration and as a result, reduce spatial resolution. Consequently, most studies focus on blood vessels with diameters above 10 μm, and include very few vessels with smaller diameters.

PCD experiments were used to evaluate the MB vibrational response within different diameter blood vessel mimicking tubes. While the two dimeters tested (280 and 100 μm) are both significantly larger than MBs, changes in MB echoes were detected, even when normalizing the results for volume within the fibers (Figure 11). Our findings suggest that stable cavitation initiates at lower sonication PNP within larger diameter fibers. In-vivo, since the sonication region is likely to include diverse diameters of blood vessels, lower PNP can be used to induce safe BBBD in larger vessel. However, at this lower PNP, reduced stable cavitation in smaller capillaries may occur, causing less BBBD in these capillaries. The ICD also increased as a function of PNP in the two fiber diameters; however, the graph's slope has a steeper incline for the smaller fibers (Figure 11). This further narrows the PNP's operational range for safe BBB opening in smaller blood vessels.

MB responses depend crucially on the excitation frequency. A center frequency of 250 kHz was used here since this is a common frequency for noninvasive brain treatment. The low frequency facilitates skull penetration due to reduced attenuation[68]. However, at this low frequency range, MB oscillations are significantly enhanced so that there is only a narrow

PNP range for safe BBBD[19]. The mechanism for these enhanced oscillations stems from the Blake threshold effect, which manifests as an infinite predicted bubble expansion beyond a critical PNP when the MBs are excited well below their resonance frequency. The PCD experiments confirm a sharp incline in MB vibrational response in both fiber diameters as a function of PNP, with a steeper slope in the smaller fibers. The current Blake threshold theory assumes that the bubbles are in free space. To fully predict MB behavior in different sized blood vessels, a modified Blake threshold effect that takes the effect of the surrounding blood vessels into account should be developed.

In-vivo, the successful implementation of the single blood vessel BBBD assessment method developed here requires the following carefully controlled protocol components: selection of US parameters (frequency, PNP and duration), titration and injection of the MBs and the two fluorescent dyes, as well as circulation times, brain harvesting, preservation, and slicing, microscopy imaging parameters, and the image processing algorithm. We showed that EB intensity increases with the microvasculature diameter, and that the fraction of vessels that undergo strong BBB openings also increases with diameter. EB was chosen here because it is a widely used molecule for BBBD visualization. However, EB is also known to diffuse quickly within the tissue. Thus, after a certain time following BBBD, the entire treated region will appear blue, and differences between blood vessels can no longer be distinguished[67]. Since EB eventually distributes across the tissue, it remains unclear whether the BBBD variations observed here at shorter time points have clinical significance. It should be noted that there are various small molecules commonly used for the assessment of BBB opening such as Dextran-tetramethylrhodamine, Alexa-fluor-cadaverine, and Texas-Red-Dextran, with spectral properties that differ from FITC[61,69]. Therefore, the same study should be repeated to examine the penetration of molecules with different sizes and diffusion coefficients.

The image processing method here was used to characterize vascular features such as vessel length and bifurcation densities in different brain areas. Variations were observed between regions, with the highest length and bifurcation density in the cortex, which is consistent with previous reports[11]. Our transducer's focal spot was large, such that most of the brain regions were insonated. Nevertheless, BBBD was observed primarily in the hypothalamus region that was also characterized here to have a low vascular density (Figures 12C, D). This suggests that vascular density may also play a significant role in BBBD, and that lower density regions may be more susceptible to BBBD (e.g., higher PNPs are required for BBBD in other regions). In the current configuration, increasing the PNP will result in damage in the form of microhemorrhages in the hypothalamus region. A smaller focal spot generated by a larger transducer aperture or a higher frequency could be used to induce BBBD more precisely, and the specific treatment parameters for each brain region can be optimized using our method.

Overall, the robust method developed here showed that BBBD depends on capillary diameter. These variations can affect the pharmacokinetics of substances that are delivered across the BBB as a function of the local microvascular content. Therefore, the impact of blood vessel diameter should be considered when developing safe and reliable protocols for FUS-mediated BBBD. It is possible that the FUS-mediated BBBD should be optimized for specific regions, vascular diameters, and vascular densities. These parameters can vary as a function of target region, animal models, and may even diverge temporarily in the same region during vasodilative or vasoconstrictive events[70]. The method here can help identify these variations and should thus be included in the arsenal of BBBD characterization protocols. Moreover, it can be used to study BBB intactness integrity as a metric to evaluate and characterize conditions and diseases that affect the BBB, such as neurodegenerative conditions, cancer, and inflammation.

7 References

1. Pardridge, W. M. The blood-brain barrier: Bottleneck in brain drug development. *Neurotherapeutics* **2**, 3–14 (2005).

2. Tung, Y.-S., Vlachos, F., Feshitan, J. A., Borden, M. A. & Konofagou, E. E. The mechanism of interaction between focused ultrasound and microbubbles in blood-brain barrier opening in mice. *J. Acoust. Soc. Am.* **130**, 3059–3067 (2011).

3. Jordão, J. F. *et al.* Antibodies Targeted to the Brain with Image-Guided Focused Ultrasound Reduces Amyloid-β Plaque Load in the TgCRND8 Mouse Model of Alzheimer's Disease. *PLoS One* **5**, e10549 (2010).

4. Curley, C. T. *et al.* Augmentation of brain tumor interstitial flow via focused ultrasound promotes brain-penetrating nanoparticle dispersion and transfection. *Sci. Adv.* **6**, eaay1344 (2022).

5. Kinoshita, M., McDannold, N., Jolesz, F. A. & Hynynen, K. Noninvasive localized delivery of Herceptin to the mouse brain by MRI-guided focused ultrasound-induced blood–brain barrier disruption. *Proc. Natl. Acad. Sci. U. S. A.* **103**, 11719 (2006).

6. Abrahao, A. *et al.* First-in-human trial of blood–brain barrier opening in amyotrophic lateral sclerosis using MR-guided focused ultrasound. *Nat. Commun.* **10**, 4373 (2019).

7. Chen, H., Brayman, A. A. & Matula, T. J. The peculiar interactions of microbubbles and microvessels. in *20th International Congress on Acoustics20th International Congress on Acoustics* (2010).

8. Caskey, C. F., Kruse, D. E., Dayton, P. A., Kitano, T. K. & Ferrara, K. W. Microbubble oscillation in tubes with diameters of 12, 25, and 195 microns. *Appl. Phys. Lett.* **88**, 033902 (2006).

9. Zheng, H. *et al.* Ultrasound-Driven Microbubble Oscillation and Translation Within Small Phantom Vessels. *Ultrasound Med. Biol.* **33**, 1978–1987 (2007).

10. Armstrong, E. Relative Brain Size and Metabolism in Mammals. *Science (80-.).* **220**, 1302–1304 (1983).

11. Todorov, M. I. *et al.* Machine learning analysis of whole mouse brain vasculature. *Nat. Methods* **17**, 442–449 (2020).

12. Wong, A. D. *et al.* The blood-brain barrier: an engineering perspective. *Front. Neuroeng.* **6**, 7 (2013).

13. Heye, A. K., Culling, R. D., Valdés Hernández, M. del C., Thrippleton, M. J. & Wardlaw, J. M. Assessment of blood–brain barrier disruption using dynamic contrast-enhanced MRI. A systematic review. *NeuroImage Clin.* **6**, 262–274 (2014).

14. Pardridge, W. M. Drug Transport across the Blood–Brain Barrier. *J. Cereb. Blood Flow Metab.* **32**, 1959–1972 (2012).

15. Saunders, N. R., Dziegielewska, K. M., Møllgård, K. & Habgood, M. D. Markers for blood-brain barrier integrity: How appropriate is Evans blue in the twenty-first century and what are the alternatives? *Front. Neurosci.* **9**, 385 (2015).

16. Xu, Y. *et al.* Quantifying blood-brain-barrier leakage using a combination of evans blue and high molecular weight FITC-Dextran. *J. Neurosci. Methods* **325**, 108349 (2019).

17. Ku, M.-C., Waiczies, S., Niendorf, T. & Pohlmann, A. Assessment of Blood Brain Barrier Leakage with Gadolinium-Enhanced MRI BT - Preclinical MRI: Methods and Protocols. in (eds. García Martín, M. L. & López Larrubia, P.) 395–408 (Springer New York, 2018).

18. Plaksin, M. *et al.* Magnetic resonance imaging analysis predicts nanoparticle concentration delivered to the brain parenchyma. *Commun. Biol.* **5**, 964 (2022).

19. Ilovitsh, T. *et al.* Enhanced microbubble contrast agent oscillation following 250 kHz insonation. *Sci. Rep.* **8**, 1–15 (2018).

20. Wood, R. W. & Loomis, A. L. The physical and biological effects of high-frequency sound-waves of great intensity. *London, Edinburgh, Dublin Philos. Mag. J. Sci.* **4**, 417–436 (1927).

21. Speed, C. A. Therapeutic ultrasound in soft tissue lesions. *Rheumatology* **40**, 1331–1336 (2001).

22. Ashokkumar, M. *et al. Handbook of Ultrasonics and Sonochemistry*. *Handbook of Ultrasonics and Sonochemistry* (Springer Singapore, 2016).

23. Hynynen, K. & Jolesz, F. A. Demonstration of Potential Noninvasive Ultrasound Brain Therapy Through an Intact Skull. *Ultrasound Med. Biol.* **24**, 275–283 (1998).

24. Krishna, V., Sammartino, F. & Rezai, A. A Review of the Current Therapies, Challenges, and Future Directions of Transcranial Focused Ultrasound Technology Advances in Diagnosis and Treatment. *JAMA Neurol.* **75**, 246–254 (2018).

25. Meng, Y., Hynynen, K. & Lipsman, N. Applications of focused ultrasound in the brain: from thermoablation to drug delivery. *Nat. Rev. Neurol.* **17**, 7–22 (2021).

26. Rayleigh, Lord. VIII. On the pressure developed in a liquid during the collapse of a spherical cavity. *London, Edinburgh, Dublin Philos. Mag. J. Sci.* **34**, 94–98 (1917).

27. Plesset, M. S. & Prosperetti, A. Bubble Dynamics and Cavitation. *Annu. Rev. Fluid Mech.* **9**, 145–185 (1977).

28. Minnaert, M. XVI. On musical air-bubbles and the sounds of running water. *London, Edinburgh, Dublin Philos. Mag. J. Sci.* **16**, 235–248 (1933).

29. Szeri, A. J., Leal, L. G., Szeri, A. J. & Leal, L. G. The onset of chaotic oscillations and rapid growth of a spherical bubble at subcritical conditions in an incompressible liquid The onset of chaotic oscillations and rapid growth of a spherical at subcritical conditions in an incompressible liquid. **551**, 1–6 (1991).

30. Leighton, T. G. 2 - Cavitation Inception and Fluid Dynamics. in (ed. Leighton, T. G. B. T.-T. A. B.) 67–128 (Academic Press, 1994).

31. Sreedhar, B. K., Albert, S. K. & Pandit, A. B. Cavitation damage: Theory and measurements – A review. *Wear* **372**–**373**, 177–196 (2017).

32. Blake, F. G. The Onset of Cavitation in Liquids. *Tech. Memo.* (1949).

33. Apfel, R. E. Acoustic cavitation prediction. *J. Acoust. Soc. Am.* **69**, 1624–1633 (1981).

34. Smirnov, I. & Mikhailova, N. An Analysis of Acoustic Cavitation Thresholds of Water Based on the Incubation Time Criterion Approach. *Fluids* **6**, 134 (2021).

35. Brennen, C. E. *Cavitation and Bubble Dynamics*. (Cambridge University Press, 2013).

36. Detsch, R. M. & Sharma, R. N. The critical angle for gas bubble entrainment by plunging liquid jets. *Chem. Eng. J.* **44**, 157–166 (1990).

37. Blomley, M. J. K. Science, medicine, and the future: Microbubble contrast agents: a new era in ultrasound. *BMJ* **322**, 1222–1225 (2001).

38. Lee, H. *et al.* Microbubbles used for contrast enhanced ultrasound and theragnosis: a review of principles to applications. *Biomed. Eng. Lett.* **7**, 59–69 (2017).

39. Marmottant, P. *et al.* A model for large amplitude oscillations of coated bubbles accounting for buckling and rupture. *J. Acoust. Soc. Am.* **118**, 3499–3505 (2005).

40. UNGER, E. C., McCREERY, T. P., SWEITZER, R. H., CALDWELL, V. E. & WU, Y. Acoustically Active Lipospheres Containing Paclitaxel. *Invest. Radiol.* **33**, 886–892 (1998).

41. Price, R. J., Skyba, D. M., Kaul, S. & Skalak, T. C. Delivery of Colloidal Particles and Red Blood Cells to Tissue Through Microvessel Ruptures Created by Targeted Microbubble Destruction With Ultrasound. *Circulation* **98**, 1264–1267 (1998).

42. Ward, M., Wu, J. & Chiu, J.-F. Ultrasound-induced cell lysis and sonoporation enhanced by contrast agents. *J. Acoust. Soc. Am.* **105**, 2951–2957 (1999).

43. Ballantine, H. T., Bell, E. & Manlapaz, J. Progress and Problems in the Neurological Applications of Focused Ultrasound. *J. Neurosurg.* **17**, 858–876 (1960).

44. Vykhodtseva, N. I., Hynynen, K. & Damianou, C. Histologic effects of high intensity pulsed ultrasound exposure with subharmonic emission in rabbit brain in vivo. *Ultrasound Med. Biol.* **21**, 969–979 (1995).

45. Hynynen, K., McDannold, N., Vykhodtseva, N. & Jolesz, F. A. Noninvasive MR Imaging–guided Focal Opening of the Blood-Brain Barrier in Rabbits. *Radiology* **220**, 640–646 (2001).

46. Sheikov, N., McDannold, N., Vykhodtseva, N., Jolesz, F. & Hynynen, K. Cellular mechanisms of the blood-brain barrier opening induced by ultrasound in presence of microbubbles. *Ultrasound Med. Biol.* **30**, 979–989 (2004).

47. Tung, Y. S., Choi, J. J., Baseri, B. & Konofagou, E. E. Identifying the inertial cavitation threshold and skull effects in a vessel phantom using focused ultrasound and microbubbles. *Ultrasound Med. Biol.* **36**, 840–852 (2010).

48. Xu, S. *et al.* Correlation Between Brain Tissue Damage and Inertial Cavitation Dose Quantified Using Passive Cavitation Imaging. *Ultrasound Med. Biol.* **45**, 2758–2766 (2019).

49. Stride, E. & Saffari, N. Theoretical and experimental investigation of the behaviour of ultrasound contrast agent particles in whole blood. *Ultrasound Med. Biol.* **30**, 1495–1509 (2004).

50. Wu, S. Y. *et al.* Transcranial cavitation detection in primates during blood-brain barrier opening-a performance assessment study. *IEEE Trans. Ultrason. Ferroelectr. Freq. Control* **61**, 966–978 (2014).

51. Kamimura, H. A. *et al.* Feedback control of microbubble cavitation for ultrasound-mediated blood–brain barrier disruption in non-human primates under magnetic resonance guidance. *J. Cereb. Blood Flow Metab.* **39**, 1191–1203 (2019).

52. Tung, Y.-S. *et al.* In vivo transcranial cavitation threshold detection during ultrasound-induced blood–brain barrier opening in mice. *Phys. Med. Biol.* **55**, 6141–6155 (2010).

53. Bismuth, M. *et al.* Acoustically Detonated Microbubbles Coupled with Low Frequency Insonation: Multiparameter Evaluation of Low Energy Mechanical Ablation. *Bioconjug. Chem.* **33**, 1069–1079 (2022).

54. Farny, C. H., Holt, R. G. & Roy, R. A. Temporal and Spatial Detection of HIFU-Induced Inertial and Hot-Vapor Cavitation with a Diagnostic Ultrasound System. *Ultrasound Med. Biol.* **35**, 603–615 (2009).

55. Corliss, B. A. *et al.* REAVER: A program for improved analysis of high-resolution vascular network images. *Microcirculation* **27**, e12618 (2020).

56. Stefanovic, B. *et al.* Functional reactivity of cerebral capillaries. *J. Cereb. Blood Flow Metab.* **28**, 961–972 (2008).

57. Bennett, R. E. *et al.* Tau induces blood vessel abnormalities and angiogenesis-related gene expression in P301L transgenic mice and human Alzheimer's disease. *Proc. Natl. Acad. Sci. U. S. A.* **115**, E1289–E1298 (2018).

58. Hall, C. N. *et al.* Capillary pericytes regulate cerebral blood flow in health and disease. *Nature* **508**, 55–60 (2014).

59. Burgess, A. *et al.* Targeted Delivery of Neural Stem Cells to the Brain Using MRI-Guided Focused Ultrasound to Disrupt the Blood-Brain Barrier. *PLoS One* **6**, e27877 (2011).

60. Lin, C. Y. *et al.* Focused ultrasound-induced blood-brain barrier opening for non-viral, non-invasive, and targeted gene delivery. *J. Control. Release* **212**, 1–9 (2015).

61. Cho, E. E., Drazic, J., Ganguly, M., Stefanovic, B. & Hynynen, K. Two-photon fluorescence microscopy study of cerebrovascular dynamics in ultrasound-induced blood–brain barrier opening. *J. Cereb. Blood Flow Metab.* **31**, 1852 (2011).

62. Nhan, T. *et al.* Drug delivery to the brain by focused ultrasound induced blood-brain barrier disruption: Quantitative evaluation of enhanced permeability of cerebral vasculature using two-photon microscopy. *J. Control. Release* **172**, 274–280 (2013).

63. Lapin, N. A., Gill, K., Shah, B. R. & Chopra, R. Consistent opening of the blood brain barrier using focused ultrasound with constant intravenous infusion of microbubble agent. *Sci. Reports 2020 101* **10**, 1–11 (2020).

64. Kubíková, T., Kochová, P., Tomášek, P., Witter, K. & Tonar, Z. Numerical and length densities of microvessels in the human brain: Correlation with preferential orientation of microvessels in the cerebral cortex, subcortical grey matter and white matter, pons and cerebellum. *J. Chem. Neuroanat.* **88**, 22–32 (2018).

65. Hase, Y. *et al.* White matter capillaries in vascular and neurodegenerative dementias. *Acta Neuropathol. Commun.* **7**, 16 (2019).

66. Poon, C., Pellow, C. & Hynynen, K. Neutrophil recruitment and leukocyte response following focused ultrasound and microbubble mediated blood-brain barrier treatments. *Theranostics* **11**, 1655–1671 (2021).

67. Xia, L. *et al.* Observation of the Blood-Brain Barrier Opening by Ultrasound with Microbubbles on Mice Using Intravital Imaging with Two-photon Microscopy. *IEEE Int. Ultrason. Symp. IUS* 2–5 (2021).

68. Hynynen, K. & Jolesz, F. A. Demonstration of potential noninvasive ultrasound brain therapy through an intact skull. *Ultrasound Med. Biol.* **24**, 275–283 (1998).

69. Yanagida, K. *et al.* Size-selective opening of the blood-brain barrier by targeting endothelial sphingosine 1-phosphate receptor 1. *Proc. Natl. Acad. Sci. U. S. A.* **114**, 4531–4536 (2017).

70. Fan, J. L. *et al.* High-speed volumetric two-photon fluorescence imaging of neurovascular dynamics. *Nat. Commun.* **11**, 1–12 (2020).

תקציר

פתיחת מחסום הדם-מוח באמצעות אולטרסאונד ומיקרובועות מהווה כלי אפקטיבי להעברת תרופות אל המוח. תנודות המיקרובועות בתגובה להפעלת האולטרסאונד וריכוזן מהווים מרכיב קריטי בהצלחת התהליך. בנוסף, כלי הדם במוח מגוונים בקוטרם, דבר שיכול להשפיע על התנהגות הבועות. השילוב שנובע מריסון של תנודות המיקרובועות בכלי דם קטנים, יחד עם כמות נמוכה יותר של מיקרובועות בכלי דם אלו עלולים ליצור שינויים בפתיחת מחסום הדם-מוח בכלי דם בקטרים שונים. במחקר זה פיתחנו שיטה לכימות המעבר של מולקולות פלורסנטיות דרך מחסום הדם-מוח לאחר פתיחתו באמצעות אולטרסאונד ומיקרובועות, כפונקציה של קוטר כלי הדם וברזולוציה של כלי דם בודד. וידוא פתיחת מחסום הדם-מוח נעשה באמצעות כימות הזליגה של צבען פלואורסנטי Evans blue (EB), בעוד שסימון כלי הדם נעשה ע"י צבען פלואורסנטי מסוג FITC דקסטרן. קוד אוטומטי לניתוח תמונות המיקרוסקופיה פותח כדי לחלץ מאפיינים צורניים של כלי הדם ולאפשר כימות ה-EB שזלג כתלות בקוטר כלי הדם. במוחות מטופלים, זליגת EB עלתה כפונקציה של קוטר כלי הדם. כמו כן, אחוז כלי הדם בהם נצפתה פתיחה של מחסום הדם-מוח, גדל כתלות בקוטר כלי הדם. לסיכום, מצאנו כי כלי דם גדולים נוטים לפתיחת מחסום הדם-מוח במידה רבה יותר לעומת כלי דם קטנים יותר. לממצא יכולות להיות השלכות על הצלחת העברת תרופות המועברות למוח באמצעות שיטה זו. לסיכום,, קוטר כלי הדם צריך להילקח בחשבון כאשר מפתחים פרוטוקולים בטוחים ואמינים לפתיחת מחסום הדם-מוח באמצעות אולטרסאונד ומיקרובועות.

אוניברסיטת תל אביב

הפקולטה להנדסה ע"ש איבי ואלדר פליישמן

בית הספר לתארים מתקדמים ע"ש זנדמן-סליינר

השפעת קוטר כלי דם מיקרוסקופים על פתיחת מחסום הדם-מוח באמצעות אולטרסאונד

חיבור זה הוגש כעבודת גמר לקראת התואר "מוסמך אוניברסיטה" בהנדסה ביו-רפואית

על-ידי

שרון כץ

העבודה נעשתה במחלקה להנדסה ביו-רפואית

בהנחיית ד"ר טלי אילוביץ'

אוניברסיטת תל אביב

הפקולטה להנדסה ע"ש איבי ואלדר פליישמן

בית הספר לתארים מתקדמים ע"ש זנדמן-סליינר

השפעת קוטר כלי דם מיקרוסקופים על פתיחת מחסום הדם-מוח באמצעות אולטרסאונד

חיבור זה הוגש כעבודת גמר לקראת התואר "מוסמך אוניברסיטה" בהנדסה ביו-רפואית

על-ידי

שרון כץ